Int. J. Plast. 163 (2023) 103553; https://doi.org/10.1016/j.ijplas.2023.103553

Geometrically necessary dislocations and related kinematic hardening in gradient grained materials: A nonlocal crystal plasticity study

Xu Zhang[1,*,†], Jianfeng Zhao[1, 2,†], Guozheng Kang[1], Michael Zaiser[3,*]

[1]*Applied Mechanics and Structure Safety Key Laboratory of Sichuan Province, School of Mechanics and Aerospace Engineering, Southwest Jiaotong University, Chengdu 610031, China.*

[2]*Institute of Systems Engineering, China Academy of Engineering Physics (CAEP), Mianyang 621999, China.*

[3]*WW8-Materials Simulation, Department of Materials Science, Friedrich-Alexander Universität Erlangen-Nürnberg, Dr.-Mack-Str. 77, 90762 Fürth, Germany.*

†These two authors contributed equally to this work.

Correspondence should be addressed to Xu Zhang; xzhang@swjtu.edu.cn, Michael Zaiser; michael.zaiser@fau.de.

Abstract

Gradient grained metals whose microstructure is characterized by a spatially graded grain size distribution show a better strength-ductility combination than their homogeneous counterparts. Kinematic hardening associated with geometrically necessary dislocations (GNDs) is considered to be a dominant strengthening mechanism in gradient grained metals. However, the precise kinematics of GND accumulation and the nature of the back stress fields remain unclear, restricting the understanding of their deformation mechanisms. In this work, a nonlocal crystal plasticity model which explicitly accounts for the interaction between dislocations and grain boundaries is developed. The nonlocal feature is achieved by introducing a flux term to account for the spatial redistribution of dislocations due to their motion. In addition, back stress produced by the spatial variation of GND density introduces an explicit internal length scale into the model. The nonlocal nature of the model on the slip system level enables the direct investigation of strain gradient effects caused by internal deformation heterogeneities. Furthermore, the interaction between dislocations and grain boundaries leads to the formation of pileups near grain boundaries, which is key to studying the grain size effects in polycrystals. Finite element implementation of the model for polycrystals with different grain sizes quantitatively captures the grain size effect. Simulation results of gradient grained materials and their homogeneous counterparts demonstrate that smaller grains lead to higher GND density and enhanced back stress. Small grains significantly contribute to the GND hardening and GND-induced kinematic hardening in gradient grained metals. This investigation helps to understand the underlying strengthening mechanisms of gradient grained metals, and the model can be readily applied to other kinds of heterogeneous materials.

Keywords: crystal plasticity; grain boundary; geometrically necessary dislocation; back stress; gradient grained material

1. Introduction

In recent years, inspired by the gradient structure in some biological materials selected by nature, gradient grained materials have been fabricated and shown to have many mechanical properties superior to their homogeneous counterparts, such as a superior strength-ductility synergy, improved fatigue and fracture resistance and enhanced frictional performance (Jiang et al., 2022a; Li et al., 2020a; Li et al., 2020b; Lu, 2014; Ma and Zhu, 2017; Wu and Zhu, 2021; Zhu and Wu, 2023). For example, Fang et al. (2011) showed that the yield strength of a gradient grained copper was about twice that of the coarse-grained one while preserving the ductility. Chen et al. (2020) reported that the coefficients of friction of a gradient nano-grained Cu-Ag alloy could be comparable to that of the nano-grained metal and remain unaltered during multiple repeated sliding. Both the low-cycle and high-cycle fatigue life were shown to be improved by introducing gradient microstructure in TWIP steel (Shao et al., 2019; Shao et al., 2017).

As a typical structural material, the microstructure of gradient grained material dominates the deformation mechanisms and the resulting macroscopic mechanical response (Ding et al., 2018; Jamalian and Field, 2020; Li et al., 2020a; Lin et al., 2018; Qin et al., 2022). Therefore, understanding the deformations mechanism is the key to correlating the microstructure with the mechanical properties. Many studies have revealed that geometrically necessary dislocations (GNDs) induced by the graded microstructure dominate the micromechanics of gradient grained materials subjecting to various loading conditions. During uniaxial tension, the nonuniform deformation-induced GNDs contribute to the strain hardening of gradient structured materials through forest hardening (Cheng et al., 2018; Wu et al., 2014a). In sliding contacts, the GNDs could result in localized microstructure change, which will influence the coefficients of friction and surface integrity of the crystalline materials (Xu et al., 2021). For gradient grained material under cyclic loading-unloading, the accumulated GNDs in the border demarcating the gradient nano-grained layer and coarse-grained core affect the local stress concentration/strain localization behavior and thus affect their fatigue life (Shao et al., 2019; Shao et al., 2017).

Apart from the aforementioned mechanisms, other strengthening and strain hardening mechanisms related to GNDs have attracted wide attention due to the fact that they are basic but important for understanding the strength-ductility synergy of gradient grained materials (Hasan et al., 2019; Moering et al., 2016; Wu et al., 2020; Wu et al., 2014b; Yang et al., 2016; Yang et al., 2015; Zhao et al., 2019; Zhao et al., 2020). Specifically, kinematic hardening (originating from back stress, which characterizes the movement of the center of the yielding surface within the paradigm of conventional plastic mechanics) was revealed to be the dominant hardening mechanism (Cheng et al., 2022; Cheng et al., 2018; Liu et al., 2018; Wang et al., 2018; Yang et al., 2016). For example, in a gradient grained interstitial-free steel, the back stress was found to contribute about 35% to the flow

stress (Yang et al., 2016). In a gradient nanotwinned metal, the back stress increased rapidly and saturated in the early deformation stage ($\varepsilon = 1\% - 2\%$); for a sample with an ultimate strength of 525 MPa, the ultimate back stress level was as high as 350 MPa (Cheng et al., 2018). Although kinematic hardening was considered a dominant strain hardening mechanism in gradient grained material, the nature of the back stress fields remains unclear and requires further study.

The graded polycrystals in gradient grained materials lead to deformation heterogeneities at two scales. At the grain scale, GNDs accumulated at grain boundaries due to the slip discontinuous among grains. These GNDs, on the one hand, act as obstacles for the movement of dislocations and thus contribute to forest hardening (a type of isotropic hardening) (Ashby, 1970); on the other hand, their spatially heterogeneous distribution gives rise to type II (inter-granular) back stress (Feaugas and Haddou, 2003; Zecevic and Knezevic, 2015; Zecevic et al., 2016), which impede further dislocation motion and provide kinematic hardening (Zhu and Wu, 2023). At the sample scale, nonuniform deformation arises due to the strain partition between coarse-grained and fine-grained layers (Jamalian and Field, 2020; Li et al., 2017; Wu et al., 2014a; Yang et al., 2015), especially for a sheet specimen, giving rise to GNDs and type I back stress, also causing isotropic hardening and kinematic hardening. In this work type III (intra-granular) back stress is not involved due to the limited strain range discussed. Currently, the prevailing view for the nature of kinematic hardening in gradient grained materials is the type I back stress. In this work, we also use the term "GND-induced kinematic hardening" to represent the kinematic hardening since it can imply the physical origin of the kinematic hardening behavior. For example, Wu et al. (2014a) experimentally observed that during the tensile deformation of a gradient grained sheet specimen, the early necking instability of the fine-grained layer introduced nonuniform lateral deformation, which should be accommodated by GNDs. These GNDs, in turn, were considered the cause of a high level of back stress. However, it was shown that during the tension of cylindrical samples in which the coarse-grained and fine-grained layer deformation is fairly compatible, the back stress is also very strong (Lee et al., 2019a; Lee et al., 2019b; Liu et al., 2018; Zhao et al., 2021). Therefore, the underlying mechanisms for back stress warrant further clarification.

To study the deformation mechanisms of metallic materials, molecular dynamics (MD) and discrete dislocation dynamics (DDD) should be preferred candidates (Fang et al., 2018; Jiang et al., 2019; Lu et al., 2022; Zhou et al., 2018). However, the attainable model sizes, grain sizes, and grain numbers are usually too restricted to match the situations in an experiment because of the heavy computational burden. For example, in MD simulations of gradient grained materials, the largest grain size was 105 nm (Li et al., 2015), much less than the grain size of the substrate in a real gradient grained sample. Therefore, the GB-related deformation mechanisms revealed by the MD simulations may differ from those in real samples. In particular, the effects of dislocation pileup

specifically concerned in heterostructured materials (Wu and Zhu, 2017; Zhu et al., 2021; Zhu and Wu, 2019) can not be well studied through MD. Furthermore, in DDD simulation, the plastic deformation was usually constrained to be smaller than 3%, restricting the revealing of the strain hardening behavior (Lu et al., 2022). In comparison, the crystal plasticity finite element method (CPFEM) usually serves as an advanced tool to investigate the effects of grain size and grain orientation on larger scales while still directly representing the spatio-temporal dynamics of dislocation-related deformation processes (Roters et al., 2019).

CPFEM based on either local or nonlocal constitutive models have been developed to study the grain size-dependent issues in metallic materials; some were also applied to gradient grained materials. The corresponding local crystal plasticity (CP) model can be classified into two types. The first type of local CP model captured the grain size effect by explicitly introducing a grain size dependent equation (e.g., Hall-Petch relation) in the constitutive law (Lu et al., 2019a; Lu et al., 2020; Wang et al., 2017; Weng, 1983; Zeng et al., 2015). This kind of model is direct and also easy to be implemented numerically. Moreover, a quantitative relationship between the microstructure and macroscopic mechanical response can be obtained. However, its rationality depends on the spatial resolution on which one envisages a constitutive model for implementation. For example, in the work of (Lu et al., 2019b; Lu et al., 2020) to deal with the relation between grain size and the macroscopic response of gradient grained material containing a large number of grains, a homogenization scheme is adopted, which allocates a grain cluster (e.g., 50 grains) to each material point. In these simulations, the direct introduction of the Hall-Petch relation would be acceptable if it is added (at the material point level) after the averaging. On the contrary, when the models are with a sub-grain resolution to represent the behavior of each material point within individual grains, the influence of grain size is a macroscopic result and should be an outcome rather than an input of the model, as also been pointed out by Haouala et al. (2018).

The second type of local CP model considered the deformation incompatibility induced slip rate/dislocation density differences in the region near and away from GB to represent the physics at GB (e.g., dislocation pileup) (Agius et al., 2022; Ghorbani Moghaddam et al., 2017; Haouala et al., 2020a; Haouala et al., 2018; Jiang et al., 2022b; Liu et al., 2020; Mayeur et al., 2015; Rubio et al., 2019). Thus the constitutive properties in regions near the GB are modified, and the GB strengthening in polycrystals can be well reflected. The advantages of this kind of model lie in that the properties of the grain boundary affected region are determined based on the dislocation pileup mechanism associated with crystallographic relationships between adjacent grains, which endow the models with more physical meanings, and sometimes even the morphology of the grain can be recognized (Agius et al., 2022). However, the grain boundary affected region usually requires an artificial length-scale parameter to characterize the region size, which is defined from different

viewpoints by different research groups. Therefore, this length-scale parameter, along with how the constitutive relations of the grain boundary affected region are defined, will influence the modeling results. In addition, the GB properties (e.g., GB strength) can not be considered in these models.

The nonlocal gradient CP model may also be classified into two categories. The first type is based on strain gradient plasticity theories (Acharya et al., 2003; Cheong et al., 2005; Dunne et al., 2007; Evers et al., 2004a, b; Evers et al., 2002; Gurtin, 2002; Haouala et al., 2020b; Lebensohn and Needleman, 2016; Lyu et al., 2017; Lyu et al., 2015; Ma et al., 2006), in which the GND density resulting from the inhomogeneous nature of plasticity in polycrystals can be calculated directly. Lower-order (Acharya and Beaudoin, 2000; Cheong et al., 2005) and higher-order (Bargmann et al., 2010) strain gradient plasticity models have been proposed to study the grain size effect in polycrystals. The lower-order models are established within the framework of classical continuum mechanics, where extra hardening due to the plastic slip gradient (or GND density) is involved in the constitutive law. The numerical approach for solving the constitutive equations is the same as that for the local models, except that the gradient term needs to be solved using ad-hoc methods, such as utilizing the derivations of the shape functions within a single element (Dai, 1997). Recently, Xu (2021) proposed a new approach to calculate the GND density based on a nonlocal domain integral to accurately represent the dislocation density near the crack tip. Compared to the lower-order models, additional higher-order stresses and boundary conditions are required in the higher-order models, which make them numerically more complicated and computationally more expensive (Gurtin, 2002). In both lower-order and higher-order strain gradient plasticity models, intrinsic material length scale(s) are introduced for dimensional consistency. Unfortunately, the values of the intrinsic material length scale(s) are usually obtained by experimental fitting and their physical meanings are still under discussion (Liu and Dunstan, 2017; Voyiadjis and Song, 2019; Zhao et al., 2022). Moreover, in some small-scale experiments where strain gradients are absent, such as the uniaxial compression of submicron/micron pillars (Greer et al., 2005), size effects were also observed, which pose issues on the strain gradient plasticity models to represent the physics of plasticity fully.

The second type of nonlocal CP model is established on the continuum dislocation dynamics (CDD) model, which describes the generation, annihilation and transportation of dislocations based on physical averages of the kinematics and dynamics of dislocations (Arsenlis et al., 2004; Groma et al., 2003; Hochrainer et al., 2014; Leung et al., 2015; Lim et al., 2011; Luscher et al., 2016; Mayeur et al., 2016; Reuber et al., 2014; Wulfinghoff and Böhlke, 2015). The transportation of dislocations among material points due to slip renders the model nonlocal. Compared to the aforementioned local models and nonlocal strain gradient-type models, a continuum representation of dislocation systems is achieved in the CDD-based CP model, by which various size effects in small-scale plasticity

caused by different mechanisms such as dislocation pileup, strain gradient and source limitation can be accounted for (Hochrainer et al., 2014). Meanwhile, no arbitrary constitutive equations or parameters are required to represent the corresponding mechanisms. The CDD theory bridges the gap between the discrete dislocation dynamics and the dislocation density-based CP model. Therefore, the scope of application of the CDD-based CP model and its computational efficiency usually lies between the discrete dislocation dynamics approach and conventional dislocation density-based CPFEM.

The capability of the models mentioned above in describing/predicting the grain size effect has been widely confirmed. However, compared to the local models that usually need ad-hoc handling on the GB, the nonlocal model naturally captures the extra hardening due to inhomogeneous plasticity (Voyiadjis and Song, 2019). Specifically, the CDD-based model physically describes the collective behavior of dislocations, which is an ideal tool for revealing the deformation mechanisms of metallic materials rather than mimicking the stress-strain relations. For gradient grained materials concerned in this work, only local models explicitly including the grain size were established to describe their macroscopic mechanical response (Lu et al., 2019b; Wang et al., 2017; Zeng et al., 2015). It stimulates this work to conduct a parsimonious modeling with minimum number of artificial parameters to clarify the nature of the back stress fields in gradient grained material. Specifically, no grain-size-related equations will be introduced into the model. Compared to existing nonlocal CP models, a major contribution of this work is that a GB model based on the dislocation-GB interaction mechanisms revealed by experiments or MD is naturally incorporated into the CPFEM framework facilitated by the dislocation transportation in CDD model, which enables us to study the GB-related problems without introducing any other ad-hoc equations to describe the dislocation density/slip rate change in the grain interior due to dislocation-GB interactions.

The rest of this paper is organized as follows: In section 2, constitutive equations and dislocation evolution laws are presented in a finite-strain framework. In section 3, the developed model is implemented into the Düsseldorf Advanced Material Simulation Kit (DAMASK) (Roters et al., 2019). Particular focus is placed on the dislocation-GB interaction in the current CP framework. In section 4, homogeneously-grained materials with different grain sizes and gradient grained materials are simulated, and the results are analyzed in detail and compared with experimental results. Finally, conclusions are presented in Section 5.

2. Constitutive model

2.1. Continuum mechanics framework

In the finite-strain description of elastic-plastic problems, the deformation kinematics is usually described in three configurations, i.e., the reference configuration, the intermediate configuration and

the current configuration. The deformation gradient tensor can be decomposed into an elastic part and a plastic part through the following multiplicative decomposition:

$$\boldsymbol{F} = \boldsymbol{F}_{\mathrm{e}} \cdot \boldsymbol{F}_{\mathrm{p}} . \tag{1}$$

The elastic part $\boldsymbol{F}_{\mathrm{e}}$ describes the elastic lattice distortion or the rigid-body rotation, and the plastic part $\boldsymbol{F}_{\mathrm{p}}$ describes the plastic deformation induced by crystallographic slip, twinning, phase transformation, etc. $\boldsymbol{F}_{\mathrm{e}}$ maps a material point from the intermediate configuration to the current configuration, $\boldsymbol{F}_{\mathrm{p}}$ maps a material point from the reference configuration to the intermediate configuration.

In the intermediate configuration, the constitutive relation can be formulated in terms of the second Piola-Kirchhoff stress $\boldsymbol{S}$ and the elastic Green-Lagrange strain tensor $\boldsymbol{E}_{\mathrm{e}}$ as

$$\boldsymbol{S} = \det\left(\boldsymbol{F}_{\mathrm{e}}\right)\boldsymbol{F}_{\mathrm{e}}^{-1} \cdot \boldsymbol{\sigma} \cdot \left(\boldsymbol{F}_{\mathrm{e}}^{-1}\right)^{\mathrm{T}} = \boldsymbol{C} : \boldsymbol{E}_{\mathrm{e}} , \tag{2}$$

where $\boldsymbol{\sigma}$ is the Cauchy stress tensor, $\boldsymbol{C}$ is the fourth-order elastic stiffness tensor, $\boldsymbol{E}_{\mathrm{e}}$ is defined as

$$\boldsymbol{E}_{\mathrm{e}} = \frac{1}{2}\left(\boldsymbol{F}_{\mathrm{e}}^{\mathrm{T}} \cdot \boldsymbol{F}_{\mathrm{e}} - \boldsymbol{I}\right). \tag{3}$$

In this work, dislocation glide is the mechanism controlling plastic deformation. The driving force for dislocation motion is the resolved shear stress on the respective slip system. Besides, back stress induced by the nonuniform spatial arrangement of dislocation may impede dislocation motion. So, the effective resolved shear stress on the slip system α is taken to be

$$\tau^{\alpha} = \boldsymbol{S} : \left(\boldsymbol{s}^{\alpha} \otimes \boldsymbol{n}^{\alpha}\right) - \tau_{\mathrm{b}}^{\alpha} , \tag{4}$$

where $\boldsymbol{s}^{\alpha}$ represents the slip direction and $\boldsymbol{n}^{\alpha}$ is the normal vector of the slip plane. The expression for back stress $\tau_{\mathrm{b}}^{\alpha}$ will be given later.

The shear rates $\dot{\gamma}^{\alpha}$ produced by the slip of dislocations on all slip systems $\alpha = 1, \ldots, N_{\mathrm{slip}}$ contribute to the plastic velocity gradient additively:

$$\boldsymbol{L}_{\mathrm{p}} = \sum_{\alpha=1}^{N_{\mathrm{slip}}} \dot{\gamma}^{\alpha} \boldsymbol{s}^{\alpha} \otimes \boldsymbol{n}^{\alpha} , \tag{5}$$

which results in the change of the plastic deformation gradient,

$$\dot{\boldsymbol{F}}_{\mathrm{p}} = \boldsymbol{L}_{\mathrm{p}} \cdot \boldsymbol{F}_{\mathrm{p}} . \tag{6}$$

The shear rate is described by the Orowan equation (Orowan, 1934),

$$\dot{\gamma}^{\alpha} = \sum_{p} \rho_{p}^{\alpha} v_{p}^{\alpha} b , \tag{7}$$

where ρ_p^α is the mobile dislocation density of type p (which will be defined in section 2.2), v_p^α is the dislocation velocity, b is the magnitude of the Burgers vector $\boldsymbol{b}$. In the following, the evolution of dislocation density and the dislocation velocity will be formulated.

2.2. Dislocation structure and dislocation density evolution

In this dislocation density-based model, the dislocation structure is characterized by the signed edge and screw dislocations and edge and screw dislocation dipoles, as defined by (Reuber et al., 2014). $c \in \{\mathrm{e}, \mathrm{s}\}$ is used to distinguish the dislocation character of either edge or screw; $p \in \{\mathrm{e}+, \mathrm{e}-, \mathrm{s}+, \mathrm{s}-\}$ further identifies the dislocation polarity. As two examples, $\rho_{\mathrm{e}+}^\alpha$ denotes the density of single positive edge dislocations on slip system α, $\rho_{\mathrm{e,dip}}^\beta$ is the density of edge dislocation dipoles on slip system β.

The total dislocation density on the slip system α is,

$$\rho^\alpha = \rho_{\mathrm{e}}^\alpha + \rho_{\mathrm{s}}^\alpha . \tag{8}$$

The total dislocation densities of edge and screw type on the same slip system are $\rho_{\mathrm{e}}^\alpha = \rho_{\mathrm{e}+}^\alpha + \rho_{\mathrm{e}-}^\alpha + \rho_{\mathrm{e,dip}}^\alpha$ and $\rho_{\mathrm{s}}^\alpha = \rho_{\mathrm{s}+}^\alpha + \rho_{\mathrm{s}-}^\alpha + \rho_{\mathrm{s,dip}}^\alpha$, respectively. With the above definitions, GND densities can be readily calculated as the absolute value of the excess densities of edge and screw characters:

$$\begin{aligned} \rho_{\mathrm{GND,e}}^\alpha &= \left| \rho_{\mathrm{e}+}^\alpha - \rho_{\mathrm{e}-}^\alpha \right| , \\ \rho_{\mathrm{GND,s}}^\alpha &= \left| \rho_{\mathrm{s}+}^\alpha - \rho_{\mathrm{s}-}^\alpha \right| , \end{aligned} \tag{9}$$

The total dipole density is the sum of the edge part and screw part:

$$\rho_{\mathrm{dip}}^\alpha = \rho_{\mathrm{e,dip}}^\alpha + \rho_{\mathrm{s,dip}}^\alpha . \tag{10}$$

Dislocation dipoles contain two dislocations with the same character but opposite signs. Thus, the formation of dipoles does not change the total dislocation density. Dipoles are stable if the distance between the two dislocations (the dipole height) does not exceed the upper bounds (Reuber et al., 2014):

$$\begin{aligned} \hat{d}_{\mathrm{e}}^\alpha &= \frac{Gb}{8\pi(1-\upsilon)\left|\tau^\alpha\right|} , \\ \hat{d}_{\mathrm{s}}^\alpha &= \frac{Gb}{4\pi\left|\tau^\alpha\right|} \end{aligned} \tag{11}$$

where G is the shear modulus, υ is Poisson's ratio. Otherwise, the dipole will dissociate under the applied stress. On the other hand, the dipole height should not be smaller than the lower bounds $\breve{d}_{\mathrm{e}}^\alpha$

and $\breve{d}_{\mathrm{s}}^{\alpha}$, under which two dislocations in the dipole will annihilate spontaneously.

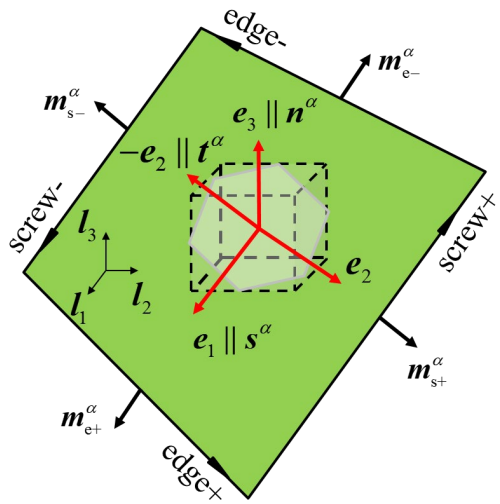

Fig. 1. Schematic of a dislocation loop on its slip plane with slip direction $\boldsymbol{s}^{\alpha}$ and normal $\boldsymbol{n}^{\alpha}$. $\boldsymbol{l}_1,\boldsymbol{l}_2,\boldsymbol{l}_3$ denote the basis of the lattice coordinate system; $\boldsymbol{e}_1,\boldsymbol{e}_2,\boldsymbol{e}_3$ are the basis of the slip system triad.

Fig. 1 shows the convention adopted in this work for the signs of dislocations, the slip direction $\boldsymbol{s}^{\alpha}$ and the slip plane normal $\boldsymbol{n}^{\alpha}$. In Fig. 1, two coordinate systems are defined: $\boldsymbol{l}_1,\boldsymbol{l}_2,\boldsymbol{l}_3$ denote the basis of the lattice coordinate system; $\boldsymbol{e}_1,\boldsymbol{e}_2,\boldsymbol{e}_3$ are the basis of the slip system triad. The expansion of the dislocation loop causes a positive shear, and the glide directions of dislocations with different characters are

$$\begin{aligned}
\boldsymbol{m}_{\mathrm{e+}}^{\alpha} &= \boldsymbol{s}^{\alpha} \\
\boldsymbol{m}_{\mathrm{e-}}^{\alpha} &= -\boldsymbol{s}^{\alpha} \\
\boldsymbol{m}_{\mathrm{s+}}^{\alpha} &= -\boldsymbol{t}^{\alpha} \\
\boldsymbol{m}_{\mathrm{s-}}^{\alpha} &= \boldsymbol{t}^{\alpha}
\end{aligned}, \tag{12}$$

where $\boldsymbol{t}^{\alpha} = \boldsymbol{s}^{\alpha} \times \boldsymbol{n}^{\alpha}$. The glide direction of a positive edge dislocation is consistent with the Burgers vector direction, i.e. $\boldsymbol{s} = \boldsymbol{b}/b$.

In the conventional dislocation density-based CP model, only dislocation multiplication and annihilation are considered. However, apart from the multiplication and annihilation of dislocations, dislocation behavior also includes the transformation between dislocation dipoles and monopolar

dislocations (change of state) and the transport of dislocations within the material. Therefore, in this work, the latter two mechanisms are also included. The dislocation density evolution laws in the following subsections are based on the work of Reuber et al. (2014), which we modify to remove some internal inconsistencies in some rate equations and to reduce the number of parameters with no physical meanings.

2.2.1 Dislocation multiplication

In the present work, dislocation generation is accomplished by loop expansion, as shown in Fig. 1. Considering that the slip of edge and screw dislocations contribute equally to the generation rates, the multiplication rate is given as

$$_{\text{mult}}\dot{\rho}_p^{\alpha} = \frac{\left(\left|\dot{\gamma}_{\text{e}^+}^{\alpha}\right| + \left|\dot{\gamma}_{\text{e}^-}^{\alpha}\right|\right) + \left(\left|\dot{\gamma}_{\text{s}^+}^{\alpha}\right| + \left|\dot{\gamma}_{\text{s}^-}^{\alpha}\right|\right)}{bk_1}\sqrt{\rho_{\text{f}}^{\alpha}}\,, \tag{13}$$

assuming that the dislocation mean free path is controlled by forest dislocations, where k_1 is a dimensionless scaling constant correlating the mean free path of dislocations with the forest dislocation spacing $1/\sqrt{\rho_{\text{f}}^{\alpha}}$. The forest dislocation density is given by $\rho_{\text{f}}^{\alpha} = \sum_{\beta=1}^{N_{\text{slip}}}\left(\rho_{\text{e}}^{\beta}\left|\boldsymbol{n}^{\alpha}\cdot\boldsymbol{t}^{\beta}\right| + \rho_{\text{s}}^{\beta}\left|\boldsymbol{n}^{\alpha}\cdot\boldsymbol{s}^{\beta}\right|\right)$.

2.2.2 Change of dislocation state

During the plastic deformation, dislocations may change their state. For example, dislocations of opposite signs can form dipoles, and dipoles will dissociate when the resolved shear stress is large enough to separate them. A dipoles is formed as two opposite dislocations capture each other. The capture occurs once an opposite-sign dislocation comes into the capture distance $2\hat{d}_c^{\alpha}$ around the captured dislocation. During the formation of dislocation dipoles, the losses of monopolar dislocation densities proposed by Reuber et al. (2014) are modified to be,

$$_{\text{sin}\to\text{dip}}\dot{\rho}_{c+}^{\alpha} = {}_{\text{sin}\to\text{dip}}\dot{\rho}_{c-}^{\alpha} = \frac{-2\hat{d}_c^{\alpha}}{b}\left(\rho_{c+}^{\alpha}\left|\dot{\gamma}_{c-}^{\alpha}\right| + \rho_{c-}^{\alpha}\left|\dot{\gamma}_{c+}^{\alpha}\right|\right). \tag{14}$$

The two terms in the bracket on the right-hand side of Eq. (14) describe reactions of two mobile dislocations of opposite signs. Note that dipoles with a height less than $\breve{d}_c^{\alpha}$ will not form; this mechanism will be considered in the dislocation annihilation part in the next section. Since the formation of dislocation dipoles does not change the total dislocation density (in this work, the total dislocation density is calculated in the manner of counting one dipole as two dislocations), the generation rate of dipole density is given by

$$ {}_{\sin\to\mathrm{dip}}\dot{\rho}^{\alpha}_{c,\mathrm{dip}} = \frac{4\hat{d}^{\alpha}_{c}}{b}\left(\rho^{\alpha}_{c+}\left|\dot{\gamma}^{\alpha}_{c-}\right| + \rho^{\alpha}_{c-}\left|\dot{\gamma}^{\alpha}_{c+}\right|\right). \tag{15} $$

Based on Eq. (11), with the increase of resolved shear stress on the slip plane, the upper bounds for the stable dislocation dipoles will decrease, leading to the dissociation of dipoles whose heights are between the "old" bounds and "new" bounds. If we assume the dipoles are distributed equally over the available heights, the changes in dipole density and mobile dislocation density due to the change of dipole heights are written in rate forms as,

$$ \begin{aligned} {}_{\mathrm{dip}\to\sin}\dot{\rho}^{\alpha}_{c,\mathrm{dip}} &= \rho^{\alpha}_{c,\mathrm{dip}}\frac{\dot{\hat{d}}^{\alpha}_{c}}{\hat{d}^{\alpha}_{c}-\breve{d}^{\alpha}_{c}} \\ {}_{\mathrm{dip}\to\sin}\dot{\rho}^{\alpha}_{c+} &= {}_{\mathrm{dip}\to\sin}\dot{\rho}^{\alpha}_{c-} = -\frac{1}{2}\rho^{\alpha}_{c,\mathrm{dip}}\frac{\dot{\hat{d}}^{\alpha}_{c}}{\hat{d}^{\alpha}_{c}-\breve{d}^{\alpha}_{c}} \end{aligned}, \tag{16} $$

where $\dot{\hat{d}}^{\alpha}_{c} = d\left(\hat{d}^{\alpha}_{c}-\hat{d}^{\alpha}_{c,\mathrm{old}}\right)\Big/dt < 0$ and $\hat{d}^{\alpha}_{c,\mathrm{old}}$ denotes the "old" dipole height. If $\dot{\hat{d}}^{\alpha}_{c} > 0$, the dipoles stay stable and the dislocation densities will not change.

2.2.3 Dislocation annihilation

The annihilation of dislocations can be classified into athermal and thermally activated ones. In this work, we aim to study the mechanical behavior of gradient grained materials at room temperature; thus, the thermally activated annihilation, such as the out-of-plane motion (climb) of edge dislocations, is ignored. Dipoles of height less than the stable height $\breve{d}^{\alpha}_{c}$ annihilate spontaneously. This process does not require thermal assistance and is different for edge and screw dipoles. Edge dipoles annihilate directly when the dipole heights are lower than $\breve{d}^{\alpha}_{c}$; while screw dipoles annihilate by cross slip, as shown in Fig. 2. Both processes can be expressed as (Reuber et al., 2014; Roters, 2011),

$$ {}_{\mathrm{athAnn}}\dot{\rho}^{\alpha}_{c,\mathrm{dip}} = -2\frac{2\breve{d}^{\alpha}_{c}}{b}\left(\rho^{\alpha}_{c+}\left|\dot{\gamma}^{\alpha}_{c-}\right| + \rho^{\alpha}_{c-}\left|\dot{\gamma}^{\alpha}_{c+}\right|\right). \tag{17} $$

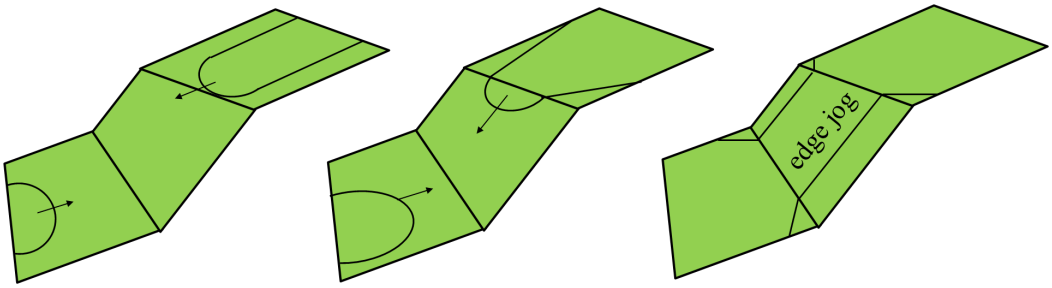

Fig. 2. Schematic of the annihilation of screw dipoles. Edge jogs are generated after the annihilation

of screw dipoles.

The annihilation of edge dipoles will leave vacancies or interstitials. In contrast, the collapse of screw dipoles by cross slip will deposit edge jogs on the collinear slip system β, as shown in Fig. 2. The length of the edge jog is equal to the average half the annihilation distance,

$$l_{\text{jog}} = \frac{\breve{d}_{\text{s}}^{\alpha}}{2}. \tag{18}$$

Assuming that the segment length of screw dipoles is in direct proportion to the mean forest dislocation spacing, the change of edge dislocation density due to the destruction of screw dipoles is,

$${}_{\text{jog}}\dot{\rho}_{\text{e+}}^{\beta} = {}_{\text{jog}}\dot{\rho}_{\text{e-}}^{\beta} = -k_2 \frac{{}_{\text{cross-slip}}\dot{\rho}_{\text{s,dip}}^{\alpha}}{2} l_{\text{jog}} \sqrt{\rho_{\text{f}}}\,, \tag{19}$$

where k_2 is a proportionality factor, ${}_{\text{cross-slip}}\dot{\rho}_{\text{s,dip}}^{\alpha} = {}_{\text{athAnn}}\dot{\rho}_{\text{s,dip}}^{\alpha}$. Besides, moving dislocations may eradicate one of the two dislocations forming a dipole, which releases the other dislocation (hence the mobile dislocation densities are unchanged) but leads to a net decrease in the dipole density,

$${}_{\text{athAnn-KO}}\dot{\rho}_{c,\text{dip}}^{\alpha} = -\frac{2\left(\hat{d}_c^{\alpha} - \breve{d}_c^{\alpha}\right)}{b} \rho_{c,\text{dip}}^{\alpha} \left(\left|\dot{\gamma}_{c-}^{\alpha}\right| + \left|\dot{\gamma}_{c+}^{\alpha}\right|\right) \tag{20}$$

2.2.4 Dislocation fluxes

The key point of this model, which makes it a nonlocal one, is the consideration of dislocation fluxes, i.e., the transport of dislocations among material points based on the kinematics of dislocations. Flux terms have been introduced into dislocation density-based CP theory by many researchers (Arsenlis et al., 2004; Hochrainer et al., 2014; Leung et al., 2015; Lim et al., 2011; Luscher et al., 2016; Mayeur et al., 2016; Wulfinghoff and Böhlke, 2015). The dislocation fluxes on the slip system α can be defined as $\boldsymbol{f}_p^{\alpha} = \rho_p^{\alpha} \boldsymbol{v}_p^{\alpha}$, where the velocities of different species are $\boldsymbol{v}_p^{\alpha} = v^{\alpha} \boldsymbol{m}_p^{\alpha}$, the scalar velocities v^{α} will be given in section 2.3. The evolution of dislocation density due to transportation among material points is given to be (Reuber et al., 2014),

$$\dot{\rho}_p^{\alpha} + \text{div}\, \boldsymbol{f}_p^{\alpha} = 0\,, \tag{21}$$

where the symbol “div” denotes the divergence of the flux.

Finally, according to Eq. (8), the total dislocation density rate $\dot{\rho}_{\text{total}}^{\alpha}$ is

$$\dot{\rho}_{\text{total}}^{\alpha} = \dot{\rho}_{\text{e+}}^{\alpha} + \dot{\rho}_{\text{e-}}^{\alpha} + \dot{\rho}_{\text{e,dip}}^{\alpha} + \dot{\rho}_{\text{s+}}^{\alpha} + \dot{\rho}_{\text{s-}}^{\alpha} + \dot{\rho}_{\text{s,dip}}^{\alpha}\,, \tag{22}$$

where the rate equations for each species can be obtained by summarizing equations (13)-(21) to obtain the following sets of partial differential equations,

$$\begin{aligned}
&\dot{\rho}^{\alpha}_{\mathrm{e+}} + \mathrm{div}\, \boldsymbol{f}^{\alpha}_{\mathrm{e+}} = {}_{\mathrm{mult}}\, \dot{\rho}^{\alpha}_{\mathrm{e+}} + {}_{\mathrm{sin}\to\mathrm{dip}}\, \dot{\rho}^{\alpha}_{\mathrm{e+}} + {}_{\mathrm{dip}\to\mathrm{sin}}\, \dot{\rho}^{\alpha}_{\mathrm{e+}} + {}_{\mathrm{jog}}\, \dot{\rho}^{\alpha}_{\mathrm{e+}} \\
&\dot{\rho}^{\alpha}_{\mathrm{e-}} + \mathrm{div}\, \boldsymbol{f}^{\alpha}_{\mathrm{e-}} = {}_{\mathrm{mult}}\, \dot{\rho}^{\alpha}_{\mathrm{e-}} + {}_{\mathrm{sin}\to\mathrm{dip}}\, \dot{\rho}^{\alpha}_{\mathrm{e-}} + {}_{\mathrm{dip}\to\mathrm{sin}}\, \dot{\rho}^{\alpha}_{\mathrm{e-}} + {}_{\mathrm{jog}}\, \dot{\rho}^{\alpha}_{\mathrm{e-}} \\
&\dot{\rho}^{\alpha}_{\mathrm{s+}} + \mathrm{div}\, \boldsymbol{f}^{\alpha}_{\mathrm{s+}} = {}_{\mathrm{mult}}\, \dot{\rho}^{\alpha}_{\mathrm{s+}} + {}_{\mathrm{sin}\to\mathrm{dip}}\, \dot{\rho}^{\alpha}_{\mathrm{s+}} + {}_{\mathrm{dip}\to\mathrm{sin}}\, \dot{\rho}^{\alpha}_{\mathrm{s+}} \\
&\dot{\rho}^{\alpha}_{\mathrm{s-}} + \mathrm{div}\, \boldsymbol{f}^{\alpha}_{\mathrm{s-}} = {}_{\mathrm{mult}}\, \dot{\rho}^{\alpha}_{\mathrm{s-}} + {}_{\mathrm{sin}\to\mathrm{dip}}\, \dot{\rho}^{\alpha}_{\mathrm{s-}} + {}_{\mathrm{dip}\to\mathrm{sin}}\, \dot{\rho}^{\alpha}_{\mathrm{s-}} \\
&\dot{\rho}^{\alpha}_{\mathrm{e,dip}} = {}_{\mathrm{sin}\to\mathrm{dip}}\, \dot{\rho}^{\alpha}_{\mathrm{e,dip}} + {}_{\mathrm{dip}\to\mathrm{sin}}\, \dot{\rho}^{\alpha}_{\mathrm{e,dip}} + {}_{\mathrm{athAnn}}\, \dot{\rho}^{\alpha}_{\mathrm{e,dip}} + {}_{\mathrm{athAnn\text{-}KO}}\, \dot{\rho}^{\alpha}_{\mathrm{e,dip}} \\
&\dot{\rho}^{\alpha}_{\mathrm{s,dip}} = {}_{\mathrm{sin}\to\mathrm{dip}}\, \dot{\rho}^{\alpha}_{\mathrm{s,dip}} + {}_{\mathrm{dip}\to\mathrm{sin}}\, \dot{\rho}^{\alpha}_{\mathrm{s,dip}} + {}_{\mathrm{athAnn}}\, \dot{\rho}^{\alpha}_{\mathrm{s,dip}} + {}_{\mathrm{athAnn\text{-}KO}}\, \dot{\rho}^{\alpha}_{\mathrm{s,dip}}
\end{aligned} \tag{23}$$

2.3. Dislocation kinetics

In order to close the system of equations, another constitutive equation is needed to specify the dislocation glide velocity. Gliding dislocations will encounter obstacles during slip. Some obstacles, such as solution particles and Peierls barriers, can be overcome with thermal assistance. In contrast, many strong obstacles can only be overcome by stress (such as forest dislocations and GBs). For dislocation-dislocation interactions, the critical shear stress $\tau^{\alpha}_{\mathrm{cr}}$ is defined. When the resolved shear stress τ^{α} is smaller than this value, dislocations cannot move; when τ^{α} surpasses this value such that the effective shear stress on the slip plane $\tau^{\alpha}_{\mathrm{eff}} = \left|\tau^{\alpha}\right| - \tau^{\alpha}_{\mathrm{cr}}$ is positive, dislocations can glide. The critical shear stress due to dislocation-dislocation interactions can be described as

$$\tau^{\alpha}_{\mathrm{cr}} = Gb\sqrt{\sum_{\alpha'=1}^{N_{\mathrm{slip}}} \xi^{\alpha\alpha'} \rho^{\alpha}}\,, \tag{24}$$

where $\xi^{\alpha\alpha'}$ describes the interaction strength between slip systems α and α'. For FCC metals, there are six interaction types among the twelve slip systems listed in Table 1, i.e., self-interaction, coplanar interaction, collinear interaction, Hirth locks, glissile junctions, and Lomer–Cottrell locks (Kubin et al., 2008). Their strengths are shown in Table 2. The interaction types between different slip systems are given in Table 3.

Table 1. Convention of slip systems for FCC materials.

α	Slip plane	Slip direction
1		$[0\ 1\ \bar{1}]$
2	$(1\ 1\ 1)$	$[\bar{1}\ 0\ 1]$
3		$[1\ \bar{1}\ 0]$
4		$[0\ \bar{1}\ \bar{1}]$

5	$(\bar{1}\ \bar{1}\ 1)$	$[1\ 0\ 1]$
6		$[\bar{1}\ 1\ 0]$
7		$[0\ \bar{1}\ 1]$
8	$(1\ \bar{1}\ \bar{1})$	$[\bar{1}\ 0\ \bar{1}]$
9		$[1\ 1\ 0]$
10		$[0\ 1\ 1]$
11	$(\bar{1}\ 1\ \bar{1})$	$[1\ 0\ \bar{1}]$
12		$[\bar{1}\ \bar{1}\ 0]$

Table 2. The interaction types and strength for FCC materials (Kubin et al., 2008).

Interaction type	Interaction coefficient
Self interaction	0.122
Coplanar interaction	0.122
Collinear interaction	0.625
Hirth lock	0.07
Glissile junction	0.137
Lomer–Cottrell lock	0.122

Table 3. The interaction types between different slip systems for FCC materials.

α / α'	1	2	3	4	5	6	7	8	9	10	11	12
1	s	cp	cp	h	l	g	cl	g	g	h	g	l
2	cp	s	cp	l	h	g	g	h	l	g	cl	g
3	cp	cp	s	g	g	cl	g	l	h	l	g	h
4	h	l	g	s	cp	cp	h	g	l	cl	g	g
5	l	h	g	cp	s	cp	g	cl	g	g	h	l
6	g	g	cl	cp	cp	s	l	g	h	g	l	h
7	cl	g	g	h	g	l	s	cp	cp	h	l	g
8	g	h	l	g	cl	g	cp	s	cp	l	h	g
9	g	l	h	l	g	h	cp	cp	s	g	g	cl
10	h	g	l	cl	g	g	h	l	g	s	cp	cp
11	g	cl	g	g	h	l	l	h	g	cp	s	cp
12	l	g	h	g	l	h	g	g	cl	cp	cp	s

Note: “s” means self-interaction, “cp” means coplanar interaction, “cl” is collinear interaction, “h” is Hirth lock, “g” means glissile junction, “l” denotes Lomer–Cottrell lock.

For pure copper studied in this work, the dislocation glide velocity is assumed to depend linearly on the effective shear stress with a mobility B,

$$v^{\alpha} = B\tau_{\mathrm{eff}}^{\alpha}. \tag{25}$$

2.4. Back stress model

Physically, the back stress comes from the spatially heterogeneous distribution of GNDs. In conventional constitutive models, the back stress is usually introduced to describe the particular mechanical behavior of materials during cyclic deformation, such as ratchetting and the Bauschinger effect (Kang and Kan, 2017). The objective of this work is to probe the effect of GND-induced kinematic hardening on the strain hardening behavior of gradient grained materials, rather than depicting the stress-strain curves. Therefore, a back stress model which is derived based on a continuum description of dislocations is employed (Groma et al., 2003),

$$\tau_{\mathrm{b}}^{\alpha} = \frac{DGb}{2\pi}\left(\frac{\mathrm{grad}_{s}\rho_{\Delta\mathrm{e}}^{\alpha}}{\rho_{\mathrm{e}}^{\alpha}\left(1-\upsilon\right)} + \frac{\mathrm{grad}_{t}\rho_{\Delta\mathrm{s}}^{\alpha}}{\rho_{\mathrm{s}}^{\alpha}}\right), \tag{26}$$

where D is a constant, which is usually taken to be 1 (Geers et al., 2009); the symbols grad_{s} and grad_{t} denote the directional derivative of $\rho_{\Delta\mathrm{e}}^{\alpha}$ and $\rho_{\Delta\mathrm{s}}^{\alpha}$ along the directions of the vectors $\boldsymbol{s}$ and $\boldsymbol{t}$, respectively. Similar forms of back stress have also been considered by Zaiser and co-workers (Zaiser and Hochrainer, 2006; Zaiser et al., 2007). Eq. (26) indicates that the back stress is related to the spatial gradient of GND density, so it is essentially proportional to a second-order strain gradient (Zaiser and Moretti, 2005). When the sample scale is of the same order of magnitude as the internal length scale, strain gradient effects become significant. Here, the internal length scale of the second-order strain gradient effect is proportional to the dislocation spacing $1/\sqrt{\rho}$, so it is expected to become relevant in regions of a few dislocation spacings around the barriers constraining dislocation motion.

3. Finite element implementation of the constitutive models and boundary conditions for dislocation flux

3.1 The integration scheme

The constitutive equations developed in this work were solved by the finite element method. In order to determine the stress necessary to achieve the prescribed deformation and update the microstructure variables as the computation time increases from $t_0 \rightarrow t$, the fully implicit integration scheme is employed. In this work, the constitutive equations are solved in the intermediate configuration, while other stress measures can be obtained by simple transformation rules. According to Eqs. (1)-(3), the second Piola-Kirchhoff stress $\boldsymbol{S}$ can be written as,

$$\boldsymbol{S}=\frac{1}{2}\boldsymbol{C}:\left(\boldsymbol{F}_{\mathrm{e}}^{\mathrm{T}}\cdot\boldsymbol{F}_{\mathrm{e}}-\boldsymbol{I}\right)=\frac{1}{2}\boldsymbol{C}:\left(\boldsymbol{F}_{\mathrm{p}}^{-\mathrm{T}}\boldsymbol{F}^{\mathrm{T}}\boldsymbol{F}\boldsymbol{F}_{\mathrm{p}}^{-1}-\boldsymbol{I}\right), \tag{27}$$

which implies that either the elastic or plastic part of the deformation gradient should be known for solving the stress. The plastic deformation gradient rate can be determined by the plastic velocity gradient $\boldsymbol{L}_{\mathrm{p}}$ as $\dot{\boldsymbol{F}}_{\mathrm{p}}=\boldsymbol{L}_{\mathrm{p}}\cdot\boldsymbol{F}_{\mathrm{p}}$, which in turn depends on the second Piola-Kirchhoff stress $\boldsymbol{S}$ driving the plastic deformation and the microstructure state variables $\boldsymbol{\omega}$, i.e.,

$$\boldsymbol{L}_{\mathrm{p}}=f\left(\boldsymbol{S},\boldsymbol{\omega}\right). \tag{28}$$

In this work, $f\left(\boldsymbol{S},\boldsymbol{\omega}\right)$ is defined by Eq. (5), and the microstructure state variables only comprise the densities of different dislocation species, as given in section 2.2. The evolution rate of the state variables depends on the current stress state and microstructures,

$$\dot{\boldsymbol{\omega}}=g\left(\boldsymbol{S},\boldsymbol{\omega}\right), \tag{29}$$

where the function $g\left(\boldsymbol{S},\boldsymbol{\omega}\right)$ has been defined elaborately in section 2.2 (Eqs. (13)-(21)). Now the remaining task is to solve Eqs. (28) and (29), with which the stress can be calculated with the deformation gradient increasing from $\boldsymbol{F}(t_0)$ to $\boldsymbol{F}(t)$, meanwhile the state variables at the end of the time step t are also updated. Since the stress and the state variables are coupling with each other, one at least has to solve a 18×18 matrix (6 for $\boldsymbol{S}$ and 12 for $\boldsymbol{\omega}$), which leads to a heavy computation burden. To resolve this problem, the set of equations can be solved using a two-level scheme alternatively:

(1) In the stress level, the stress is solved by solving Eqs. (6), (27), (28) at a constant state $\boldsymbol{\omega}$.

(2) In the microstructure level, the state $\boldsymbol{\omega}$ is solved by solving Eq. (29) for a given stress $\boldsymbol{S}$.

(1) Stress level integration

To sovle Eqs. (6), (27), (28) for the time integration of stress, Eq. (6) can be written as ,

$$\frac{\boldsymbol{F}_{\mathrm{p}}\left(t\right)-\boldsymbol{F}_{\mathrm{p}}\left(t_0\right)}{\Delta t}=\boldsymbol{L}_{\mathrm{p}}\left(t\right)\boldsymbol{F}_{\mathrm{p}}\left(t\right), \tag{30}$$

the deformation gradients at the end of the increment can be given as,

$$\begin{aligned}\boldsymbol{F}_{\mathrm{p}}\left(t\right)&=\left(\boldsymbol{I}-\Delta t\boldsymbol{L}_{\mathrm{p}}\left(t\right)\right)^{-1}\boldsymbol{F}_{\mathrm{p}}\left(t_0\right)\\ \boldsymbol{F}_{\mathrm{e}}\left(t\right)&=\boldsymbol{F}\left(t\right)\boldsymbol{F}_{\mathrm{p}}^{-1}\left(t_0\right)\left(\boldsymbol{I}-\Delta t\boldsymbol{L}_{\mathrm{p}}\left(t\right)\right)\end{aligned}. \tag{31}$$

The second Piola-Kirchhoff stress at the end of the increment is thus,

$$\boldsymbol{S}\left(t\right)=\frac{1}{2}\boldsymbol{C}:\left\{\underbrace{\left[\boldsymbol{I}-\Delta t\boldsymbol{L}_{\mathrm{p}}^{\mathrm{T}}\left(t\right)\right]}_{\boldsymbol{B}^{\mathrm{T}}}\underbrace{\boldsymbol{F}_{\mathrm{p}}^{-\mathrm{T}}\left(t_0\right)\boldsymbol{F}^{\mathrm{T}}\left(t\right)\boldsymbol{F}\left(t\right)\boldsymbol{F}_{\mathrm{p}}^{-1}\left(t_0\right)}_{\boldsymbol{A}}\underbrace{\left[\boldsymbol{I}-\Delta t\boldsymbol{L}_{\mathrm{p}}^{\mathrm{T}}\left(t\right)\right]}_{\boldsymbol{B}}-\boldsymbol{I}\right\}. \tag{32}$$

The stress level integration is done by using the Newton–Raphson scheme, where $\boldsymbol{F}_{\mathrm{e}}$, $\boldsymbol{L}_{\mathrm{p}}$ and $\boldsymbol{S}$ can be chosen as the objective for integration. Since a small change in $\boldsymbol{S}$ results in an enormous change in $\boldsymbol{L}_{\mathrm{p}}$, the Newton–Raphson scheme is built around $\boldsymbol{L}_{\mathrm{p}}$. The residual of $\boldsymbol{L}_{\mathrm{p}}$ after *n* iterations can be written as,

$$\boldsymbol{R}_n = \tilde{\boldsymbol{L}}_{\mathrm{p},n} - f\left(\boldsymbol{S}\left(\boldsymbol{F}_{\mathrm{e}}\left(\tilde{\boldsymbol{L}}_{\mathrm{p},n}\right)\right), \boldsymbol{\omega}\right), \tag{33}$$

where $\tilde{\boldsymbol{L}}_{\mathrm{p},n}$ is the guess value for $\boldsymbol{L}_{\mathrm{p}}$ and $f\left(\boldsymbol{S}\left(F_{\mathrm{e}}\left(\tilde{\boldsymbol{L}}_{\mathrm{p},n}\right)\right), \boldsymbol{\omega}\right)$ is the value calculated by the constitutive model. The Newton–Raphson scheme is employed to obtain $\boldsymbol{L}_{\mathrm{p}}$ at iteration *n*+1,

$$\begin{aligned} \boldsymbol{R}_n &= \tilde{\boldsymbol{L}}_{\mathrm{p},n} - f\left(\boldsymbol{S}\left(\boldsymbol{F}_{\mathrm{e}}\left(\tilde{\boldsymbol{L}}_{\mathrm{p},n}\right)\right), \boldsymbol{\omega}\right) \\ \tilde{\boldsymbol{L}}_{\mathrm{p},n+1} &= \tilde{\boldsymbol{L}}_{\mathrm{p},n} - \left(\frac{\partial \boldsymbol{R}_n}{\partial \tilde{\boldsymbol{L}}_{\mathrm{p}}}\right)^{-1} : \boldsymbol{R}_n \end{aligned} . \tag{34}$$

The term $\partial \boldsymbol{R}_n / \partial \tilde{\boldsymbol{L}}_{\mathrm{p}}$ is calculated as,

$$\frac{\partial \boldsymbol{R}_n}{\partial \tilde{\boldsymbol{L}}_{\mathrm{p}}} = \boldsymbol{I} \otimes \boldsymbol{I} - \frac{\partial f}{\partial \boldsymbol{S}} \frac{\partial \boldsymbol{S}}{\partial \tilde{\boldsymbol{L}}_{\mathrm{p}}}, \tag{35}$$

where $\partial f / \partial \boldsymbol{S}$ is known from the constitutive law (Eq. (28)), and $\partial \boldsymbol{S} / \partial \tilde{\boldsymbol{L}}_{\mathrm{p}}$ is given as,

$$\frac{\partial \boldsymbol{S}}{\partial \tilde{\boldsymbol{L}}_{\mathrm{p}}} = -\frac{\Delta t}{2} \boldsymbol{C} : \left(\frac{\partial \tilde{\boldsymbol{L}}_{\mathrm{p}}^{\mathrm{T}}}{\partial \tilde{\boldsymbol{L}}_{\mathrm{p}}} \boldsymbol{A}\boldsymbol{B} + \boldsymbol{B}^{\mathrm{T}} \boldsymbol{A}\left(\boldsymbol{I} \otimes \boldsymbol{I}\right) \right). \tag{36}$$

The iteration is considered to be converged when all components of $\boldsymbol{R}_n$ are below a given tolerance.

(2) Microstructure level integration

The second level of integration updates the state variables for a given stress $\boldsymbol{S}$. Different schemes can be employed to do this. Kords (2013) has compared the performance of several integration schemes such as explicit Euler integrator, adaptive Euler integrator, fourth-order explicit Runge-Kutta integrator and fifth-order adaptive Runge-Kutta integrator. It is found that the adaptive Euler integrator performed best for different constitutive models taking into account the computation efficiency and accuracy. Therefore, the adaptive Euler integration scheme is used in this work for solving the state variables $\boldsymbol{\omega}$. This integrator is essentially an enhancement of the explicit Euler integrator, while the error is estimated by evaluating the state variables again after the stress integration. Based on Eq. (29), $\boldsymbol{\omega}$ at the end of the increment can be given as

$$\boldsymbol{\omega}\left(t\right) = \boldsymbol{\omega}\left(t_0\right) + g\left(\boldsymbol{S}\left(t_0\right), \boldsymbol{\omega}\left(t_0\right)\right)\Delta t \tag{37}$$

using the explicit Euler integrator. For the adaptive Euler integrator, $\boldsymbol{\omega}$ is further calculated by integrating the stress again using the known $\boldsymbol{\omega}(t)$ and recalculated $\boldsymbol{S}(t)$, i.e.,

$$\tilde{\boldsymbol{\omega}}(t) = \boldsymbol{\omega}(t_0) + g\left(\boldsymbol{S}(t), \boldsymbol{\omega}(t)\right)\Delta t \,. \tag{38}$$

The error is defined as,

$$\xi = \frac{\tilde{\boldsymbol{\omega}}(t) - \boldsymbol{\omega}(t)}{2}, \tag{39}$$

which is compared to a given tolerance to determine the convergence of the iteration.

The dislocation density change due to flux (as given in section 3.2) is updated immediately after every update of dislocation densities due to multiplication, change of state and annihilation. With the above schemes for stress integration and state variables update, the procedure for solving the constitutive equations can be summarized by the flow chart below,

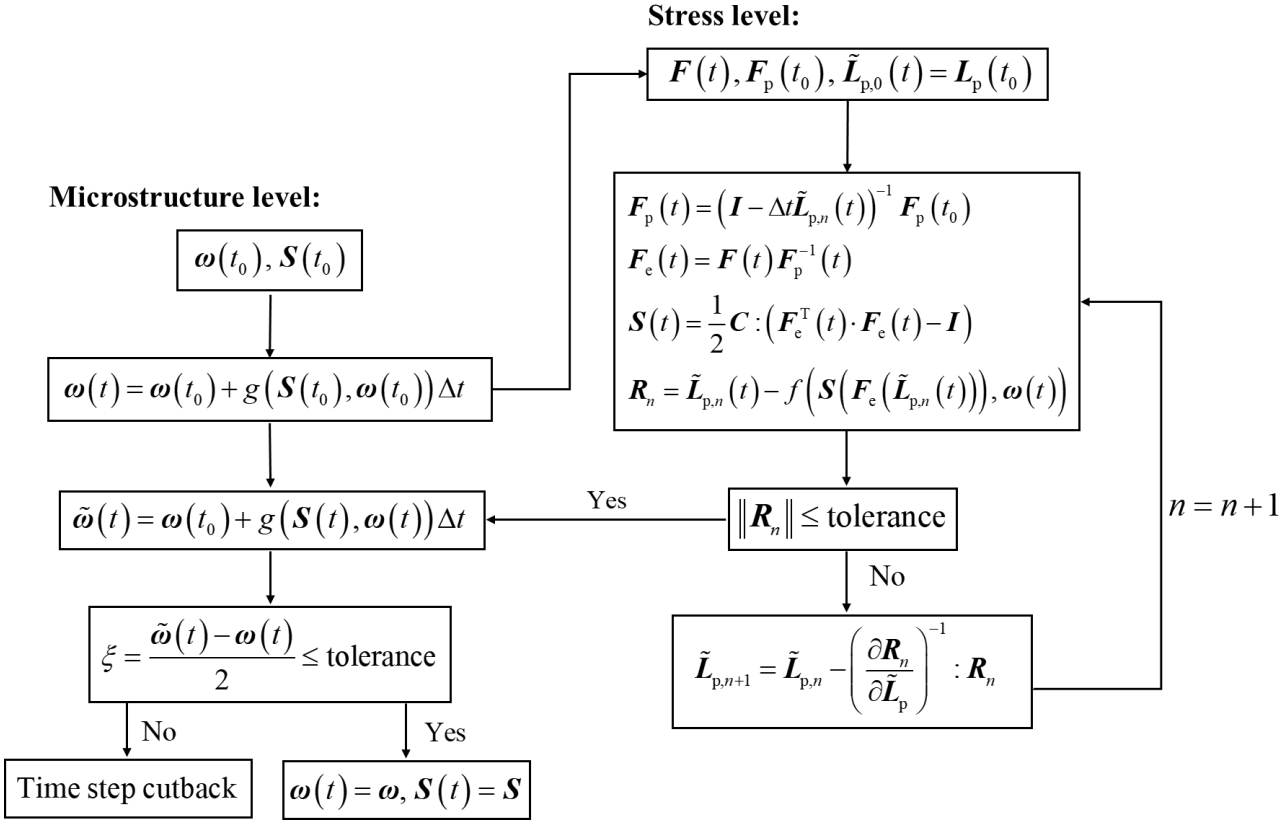

Fig. 3. Flow chart for numerically solving the constitutive equations.

3.2 Finite volume upwind scheme for solving dislocation flux

In this work, the finite volume upwind scheme is employed for solving the transport equation (Eq. (21)). Furthermore, additional boundary conditions for dislocation fluxes, which are key to the interface-dominated mechanical response, will also be given in detail.

To numerically solve the flux function, the body is discretized into grid points (corresponding to integration points in the finite element method) where each grid point is associated with a "control

volume", as shown in Fig. 4. By using the divergence theorem over the control volume surrounding the material point, the volume integral of the flux divergence

$$\int_V \operatorname{div} \boldsymbol{f}_p^\alpha \, \mathrm{d}V = \int_{\partial V} \boldsymbol{f}_p^\alpha \cdot \boldsymbol{a}^n \, \mathrm{d}a = \sum_n \tilde{\boldsymbol{f}}_p^\alpha \cdot \boldsymbol{a}^n A^n = V \operatorname{div} \tilde{\boldsymbol{f}}_p^\alpha , \tag{40}$$

is calculated as the sum of average fluxes $\tilde{\boldsymbol{f}}_p^\alpha$ over all surfaces n with outward unit normal vector $\boldsymbol{a}^n$ and area A^n. Then, Eq. (21) can be rewritten as,

$$\dot{\rho}_p^\alpha + \frac{1}{V} \sum_n \tilde{\boldsymbol{f}}_p^\alpha \cdot \boldsymbol{a}^n A^n = 0 . \tag{41}$$

Now the interfaces can be sorted, i.e., dislocations flow in through some interfaces and flow out through the remaining ones.

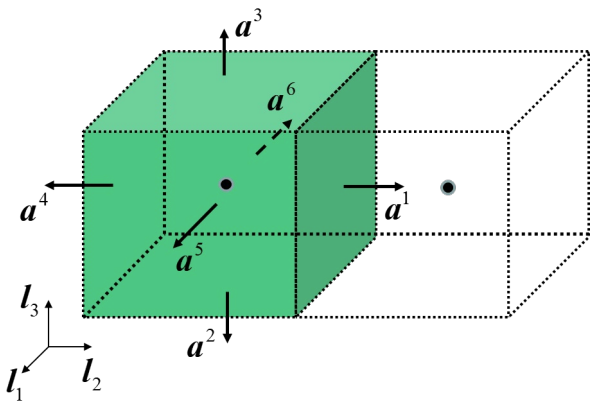

Fig. 4. Control volume with basis triad $\boldsymbol{l}_1, \boldsymbol{l}_2, \boldsymbol{l}_3$ for each material point. $\boldsymbol{A}^n$ ($n \in [1,6]$) represent the outward unit normal vectors of the six surfaces.

Fluxes $\boldsymbol{f}_p^\alpha$ of all mobile dislocation species are evaluated at the center of the control volumes. If dislocations in the concerned control volume flow out through surface n into an adjacent control volume, $\boldsymbol{f}_p^\alpha \cdot \boldsymbol{a}^n > 0$, then $n \in S_{\text{out}}^{\alpha,p}$ and the boundary flux is set to $\tilde{\boldsymbol{f}}_p^\alpha = \boldsymbol{f}_p^\alpha$; if dislocations flow in through surface n, $\boldsymbol{f}_p^{\alpha,n} \cdot \boldsymbol{a}^n < 0$, then $n \in S_{\text{in}}^{\alpha,p}$ and the boundary flux is set to $\tilde{\boldsymbol{f}}_p^\alpha = \boldsymbol{f}_p^{\alpha,n}$, where $\boldsymbol{f}_p^{\alpha,n}$ is evaluated at the grid point of the adjacent control volume. With these definitions, we have

$$\text{flux}\, \dot{\rho}_p^\alpha = - \underbrace{\frac{1}{V} \sum_{n \in S_{\text{out}}^{\alpha,p}} \boldsymbol{f}_p^\alpha \cdot \boldsymbol{a}^n A^n}_{\text{flux out}} - \underbrace{\frac{1}{V} \sum_{n \in S_{\text{in}}^{\alpha,p}} \boldsymbol{f}_p^{\alpha,n} \cdot \boldsymbol{a}^n A^n}_{\text{flux in from adjacent control volumes}} , \tag{42}$$

by which the rate form of the dislocation density change due to dislocation flux is given explicitly. Note that during finite element implementation the time step has to meet the CFL (Courant-

Friedrichs-Lewy) condition of $\Delta t < \sqrt[3]{V}/v$. This condition ensures that dislocations are, in any time step, only exchanged among adjacent integration points.

3.3 Boundary conditions for dislocation fluxes

In polycrystals, moving dislocations will encounter interfaces (e.g., GBs) that stop them or free surfaces where they can leave without surface passivation (Hua et al., 2021). Therefore, additional boundary conditions have to be specified to complete the boundary value problem when dislocation fluxes are involved. In the current work, two common cases, i.e., dislocation-GB interactions and dislocation-surface interactions, are considered for polycrystalline metals. The latter can be treated straightforwardly within the above transport scheme by computing the fluxes out of a surface in the same manner as in a bulk control volume; meanwhile, there are no inbound fluxes through the surface(s) that coincide with the surface of the material body. In contrast, dislocation-GB interactions are more complex and will be discussed in detail.

Considering a polycrystal in which GBs are free of pre-existing dislocations, once a sequence of dislocations is pushed against a GB, dislocations are stopped and form pileups. When the shear stress at the tip of a pileup reaches a critical value, the leading dislocation will be absorbed by the GB or "transmitted" through the GB, i.e., emitting another dislocation to the adjacent gain. Both processes generate ledges on the GB. In the present work, the interactions of dislocations with GB are considered in the form of blocking and transmission. The continuous absorption of dislocations at GBs without emission is not considered since the grain boundaries will become unstable; thus, they need to emit dislocations to release the local high energy, which implies a transmission process. Therefore, the transmission, which can be treated as a combination of absorption (annihilation) and emission (nucleation), is employed. That is to say, the annihilation and nucleation of dislocations at GBs are considered in this work, but in a more suitable way under the assumption that grain boundaries are at a stable state. The boundary condition for blocking is simply imposed by setting, in a GB adjacent voxel (control volume shown in Fig. 4), the flux through the control volume surface that coincides with the GB equals zero. The mathematical description for transmission is given below.

It can be concluded from the review paper (Bayerschen et al., 2016) that for modeling dislocation transmission through GB, three dominant factors have to be considered: the orientation relationship between grains, the Burgers vector magnitude of the debris deposited in the GB, the resolved shear stress on the outgoing slip system. In MD simulations, the shear stress is relatively high because alternative plastic relaxation mechanisms are absent; therefore, GB barriers can be readily overcome. In DDD simulations parameterized by MD, GBs can also be overcome by means of local stress concentrations, which lead to local stresses at the GB that may substantially exceed the average stress in the grain. In the currently adopted CP method, such stress concentrations are

averaged out; hence the stress fields are too smooth to produce the required local stress concentrations for dislocations to be transmitted through GBs so that dislocations remain stuck. However, this does not mean that the CP modeling cannot capture the transmission process. In fact, one can learn from experimental results and small-scale simulations in conjunction with statistical arguments to derive conditions for dislocation transmission in the CP framework.

Recent experimental results (Bieler et al., 2019) showed that for aluminum polycrystals with near-cube oriented grains, slip transfer across GBs is only consistently evident when the misorientation angles between grains are less than 15°. When misorientation angles are higher than 15°, slip transfer was only occasionally observed. Alizadeh et al. (2020) also showed that slip transfer is more likely to occur when the Luster–Morris parameter (the definition can be found in the referenced paper) is larger than 0.9, and the magnitude of the residual Burgers vector is less than 0.35*b*. These experimental findings indicate that whether a dislocation can transmit through GB is a probabilistic event rather than an absolute one. These experimental results can be well interpreted by existing experimental measurements (Wilkinson et al., 2014), numerical simulations (Groma and Bakó, 1998; Wilkinson et al., 2014) and theoretical derivations (Groma and Bakó, 1998; Zaiser and Seeger, 2002), which show that the stress field created by an ensemble of randomly distributed dislocations is stochastic and can be described by a probability density function with a Gaussian center and asymptotic power-law tails. High local shear stresses in the tails of the distribution will be present with sufficient probability to locally assist dislocation transmission through GBs. The tails of the probability density function of local shear stress are given by (Groma and Bakó, 1998)

$$P = \frac{CG^2b^2\rho}{(\tau - \langle\tau\rangle)^3}, \tag{43}$$

where C is a factor of the order of unity that depends on the line orientation and Burgers vector distribution of the dislocations that generate the internal stress field; the first moment of this probability density function is the mesoscopic shear stress $\langle\tau\rangle$, which can be calculated in the CP framework. The density function is symmetrical around this $\langle\tau\rangle$. The tails in the scenario mentioned above describe the probability density of stress close to dislocation lines.

In the CP framework where dislocations are assumed to be randomly distributed inside each material point, whether dislocations can be transmitted through GBs depends greatly on the local stress facing the GB. Based on the above discussions, the transmission probability can be considered as the probability that the local stress is larger than the GB strength $\tau^{\alpha}_{\mathrm{c,\,trans}}$. Therefore, instead of considering a specific dislocation arrangement and calculating the shear stress e.g. at the tip of a

pileup, which is what happens by default in DDD simulations, we consider in this CDD framework that once a dislocation impinges on the GB, it transmits through the GB with probability $P_{\text{trans}} \in [0,1]$. The transmission probability can be obtained by integration of Eq. (43),

$$P_{\text{trans}} = \frac{CG^2b^2\rho}{2}\left[\frac{1}{\left(\tau^{\alpha}_{\text{c, trans}} - \tau^{\alpha}\right)^2} + \frac{1}{\left(\tau^{\alpha}_{\text{c, trans}} + \tau^{\alpha}\right)^2}\right], \tag{44}$$

where the local stress average $\langle\tau\rangle$ is equated with the shear stress τ^{α} evaluated from the CP framework. The critical strength for dislocation transmission through GBs is determined as (Fan et al., 2011; Li et al., 2009)

$$\tau^{\alpha}_{\text{c, trans}} = \frac{E_{\text{GB}}b^{\alpha}_{\text{in}} + \eta G\left(b^{\alpha}_{\text{ledge}}\right)^2}{\left(b^{\alpha}_{\text{in}}\right)^2}, \tag{45}$$

where E_{GB} is the GB energy, which depends on the GB type, materials properties, the misorientation angle between adjacent grains, etc. In this work, we consider the general GBs, and the GB energy is calculated using the method proposed by Bulatov et al. (2014), which has been implemented into the current CPFEM framework. $b^{\alpha}_{\text{ledge}}$ is the magnitude of Burgers vector of the GB ledge, b^{α}_{in} denotes that of the incoming dislocation, η is a constant taken to be 0.5 (Hull and Bacon, 2001).

With probability $1-P_{\text{trans}}$ a dislocation is blocked. For a dislocation that transmits through a GB, a geometric criterion needs to be constructed to determine the slip plane and slip direction of the corresponding outgoing dislocation. TEM observations (Lee et al., 1989) showed that the orientation relationship between the incoming and outgoing slip plane, the magnitude of Burgers vector of the residual dislocation and the resolved shear stress on the outgoing slip system co-determine the character of the outgoing dislocation. It was further demonstrated that if the resolved shear stress on one outgoing slip system is maximum among all slip systems, but the transmission leaves a ledge with a large Burgers vector on the GB, this process will eventually cease to operate. Therefore, the following conditions are adopted in this work to determine the outgoing slip systems:

(1) The angle between the traces of the incoming and outgoing slip planes on the GB, i.e., $\left|\boldsymbol{l}^{\alpha}_{\text{A}}\cdot\boldsymbol{l}^{\beta}_{\text{B}}\right|$ shown in Fig. 5, should be minimum.

(2) The magnitude of the Burgers vector of the residual dislocation $\left|\boldsymbol{b}_{\text{in}} - \boldsymbol{b}_{\text{out}}\right|$ is minimum.

(3) The outgoing slip system has operated, while the resolved shear stress on the outgoing slip

system is not necessarily maximum, i.e., $\tau_{\text{eff}}^{\beta} > 0$.

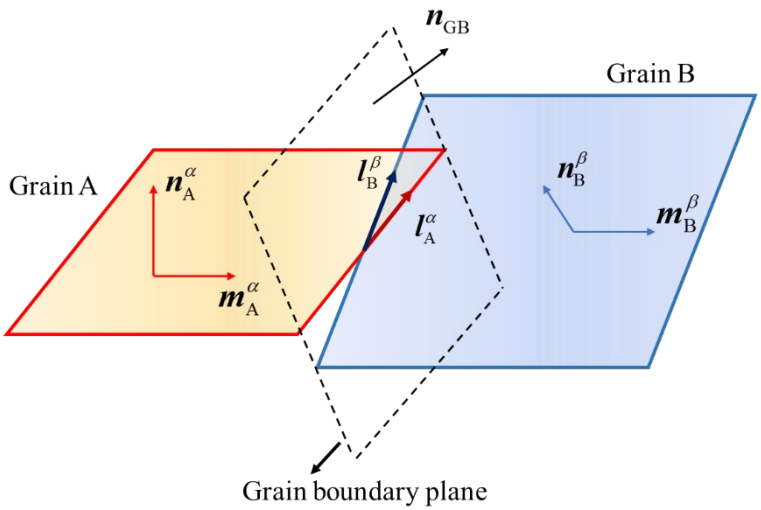

Fig. 5. Schematic of two slip systems α, β in adjacent grains A and B.

The above GB-dislocation interaction mechanisms have been implemented into the CPFEM framework by serving as boundary conditions for dislocation transport, while no ad-hoc equations were required to describe the GB hardening. This allows us to study the GB-related deformation mechanisms and macro/micro-mechanical response of both homogeneous polycrystals and gradient grained polycrystals directly and physically.

4. Uniaxial tensile response of homogeneously-grained copper

4.1. Finite element model

In order to study the mechanical properties of gradient grained materials, the tensile responses of homogeneously-grained polycrystals are simulated at first to validate and parameterize the developed model. In this work, the 2D model is employed to ease the computation burden, which comes from two aspects (Kords, 2013). Firstly, for numerically solving the dislocation transport term, the finite volume upwind scheme is used, i.e., the spatial domain is discretized into a number of voxels. Therefore, to ensure that no dislocation can move further than the next neighboring voxel within one time step, the time step should be limited to satisfy the condition of $\Delta t = \sqrt[3]{V}/v$, where V is the volume of the voxel and v is the dislocation velocity. This limitation reduces the computation efficiency, i.e., the time step needed to integrate the state is generally much smaller than the time step required by the mechanical boundary value solver. Secondly, due to the non-locality of the constitutive model, the integration of one material point depends on those of its neighboring material points. Specifically, if an integration point does not converge and has to do a timestep cutback, then

all neighbors have to do cutbacks as well to ensure that non-converged integration points are always surrounded by a layer of already converged integration points. This will further reduce the computation efficiency. Therefore, to reduce the computation cost, we use 2D models in the current simulation. Kords (2013) also adopted a 2D model (with only one element along the *Z* direction) to simulate an indentation problem by using the original version of the constitutive model employed in this work. In the future, the FFT approach will be combined with the current model to promote computation efficiency, as in Refs. (Haouala et al., 2020b; Lebensohn and Needleman, 2016).

Therefore, representative volume elements (RVEs) consisting of 50 randomly oriented grains were employed for homogeneously-grained materials, as shown in Fig. 6. The model was generated using the Voronoi algorithm by the open-source software Neper (Quey et al., 2011), and discretized with $40\times40\times1$ ($x\times y\times z$) 8-node brick elements with reduced integration (C3D8R). The mesh convergence study demonstrates that the mesh resolution adopted here is sufficiently high for the homogeneous polycrystals studied, as shown in the Appendix. To simulate the uniaxial tensile deformation, displacement constraints of Uy=0 and Ux=0 were applied on the lower surface (negative x-z plane) and left surface (negative y-z plane), respectively, and uniaxial tension was applied on the right surface (positive y-z plane) along x-direction at a strain rate of $6\times10^{-4}/\mathrm{s}$. Displacements and dislocation fluxes were not allowed along the z-direction.

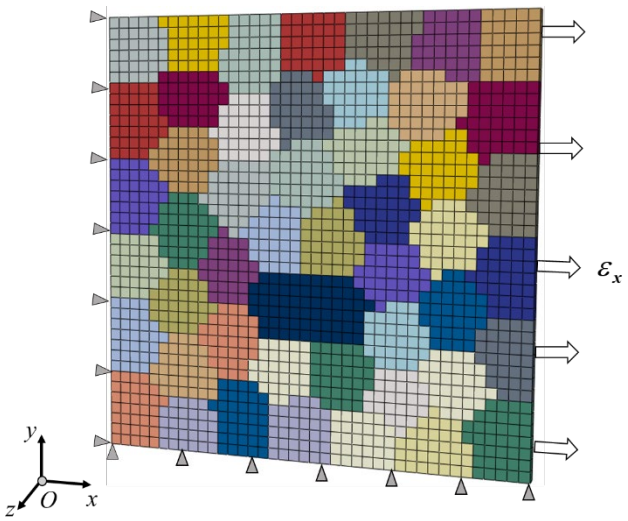

Fig. 6. RVE containing 50 randomly orientated grains generated using the Voronoi algorithm. The RVE was discretized with 40×40×1 ($x\times y\times z$) hexahedron elements during finite element simulation.

4.2. Validation of the constitutive model and parameter calibration

Fig. 7 shows the simulation results for homogeneous copper polycrystals with grains sizes

ranging from 5 μm to 80 μm. The material parameters adopted for this constitutive model are summarized in Table 4, most of which have clear physical meanings or clear physical bounds. The elastic constants are obtained from the work of Luscher et al. (2013). The magnitude of the Burgers vector is given by Espinosa et al. (2006). Essmann and Mughrabi (1979) showed that the stable edge dipole and screw dipole heights are 6*b* and 200*b*-2000*b*. In this work, we take 6*b* for the edge dipole and 200*b* for the screw dipole, respectively, as adopted by Grilli et al. (2018). The strength of the Peierls barrier is given as 0.5 MPa (Grilli, 2016). The edge jog parameter k_2 can be determined by referring to the work of Kords (2013) on aluminum and nickel. The dislocation mobility B controls the dislocation velocity, and it has been validated that the simulation results show negligible difference for $B \leqslant 10$ Pa·s. So B is set to be 10 Pa·s in this work to promote computation efficiency. The remaining two parameters, which obviously affect the simulation results, are the dislocation multiplication coefficient and the initial dislocation density. In this work, every type of monopolar dislocation density on each slip system is set to be $2.5\times10^{10}/\mathrm{m}^2$, and the dipole density is set to be 0, leading to a total dislocation density of $\rho_{\text{initial}} = 1.2\times10^{12}/\mathrm{m}^2$ at every material point, which is the same as that adopted in (Haouala et al., 2020b; Haouala et al., 2018) for modeling the Hall-Petch effect of polycrystalline FCC metals. The dislocation multiplication coefficient k_1 ($10 \le k_1 \le 100$) is taken to be 50 to mimic the experimental results.

Table 4. Parameters for the nonlocal constitutive model.

Parameter	Symbol	Value	Reference
Elastic constants (Pa)	C_{11}	168×10^9	(Luscher et al., 2013)
	C_{12}	121.4×10^9	(Luscher et al., 2013)
	C_{44}	75.3×10^9	(Luscher et al., 2013)
Initial dislocation densities ($\mathrm{m/m^3}$)	ρ_p^0	2.5×10^{10}	
Initial dipole densities ($\mathrm{m/m^3}$)	$\rho_{c,\mathrm{dip}}^0$	0	
Magnitude of the Burger vector (m)	b	2.56×10^{-10}	(Espinosa et al., 2006)
Lower bound for edge dipole (m)	$\check{d}_{\mathrm{e}}$	1.536×10^{-9}	(Essmann and Mughrabi, 1979)
Lower bound for screw dipole (m)	$\check{d}_{\mathrm{s}}$	51.2×10^{-9}	(Essmann and Mughrabi, 1979)
Dislocation multiplication coefficient	k_1	50	
Edge jog parameter	k_2	0.01	(Kords, 2013)
Dislocation viscosity (Pa·s)	B	10	

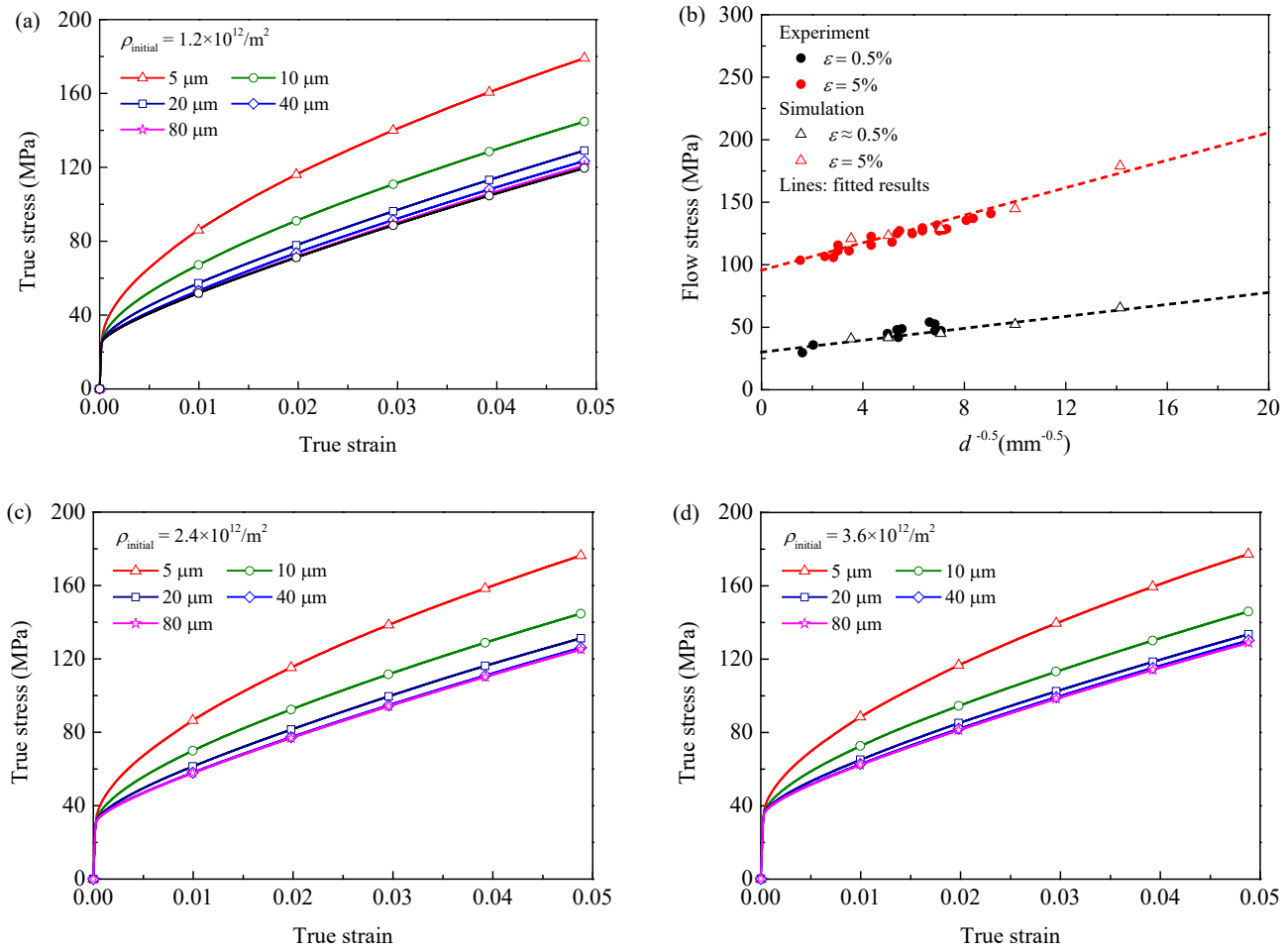

Fig. 7. (a) Simulated results of homogeneous copper polycrystals with grain sizes changing from 5 μm to 80 μm with initial dislocation density of $1.2\times10^{12}/m^2$. (b) Comparison of the simulation results with experimental ones (Armstrong et al., 1962; Hansen and Ralph, 1982) at the true strains of 0.5% and 5%, with initial dislocation density of $1.2\times10^{12}/m^2$. (c) and (d) Simulated results of homogeneous copper polycrystals with initial dislocation densities of $2.4\times10^{12}/m^2$ and $3.6\times10^{12}/m^2$.

Fig. 7(a) manifests that the flow stress increases gradually with the decrease of grain size. Thus the developed model can predict the grain size effect without inducing any grain size-dependent parameters. When the grain size increases above 40 μm, the simulation stress-strain curves show little difference, indicating that the grain size effect becomes rather weak, and the mechanical responses can be described by a local constitutive model in this grain size range. By further comparing with experimental results (Armstrong et al., 1962; Hansen and Ralph, 1982), the simulation results quantitatively capture the grain size effect for copper polycrystals at the true strains of 0.5% and 5%, i.e., the flow stress increases linearly with the increase of $d^{-0.5}$, as shown in

Fig. 7(b). The above results indicate that the developed model can be utilized to study grain size-dependent problems such as the gradient grained structure concerned in this work with few adjustable parameters.

Figs. 7(c) and 7(d) further give the tensile response of copper polycrystals with initial dislocation densities of $\rho_{\text{initial}} = 2.4\times10^{12}/\text{m}^2$ and $\rho_{\text{initial}} = 3.6\times10^{12}/\text{m}^2$, respectively. Comparing Figs. 7(a), 7(c) and 7(d), it is found that the initial flow stress of copper polycrystals depends both on the grain size and initial dislocation density. Specifically, the elastic limit of the copper polycrystals only depends on the initial dislocation density since the dislocation motion is controlled by the Taylor hardening law (Eq. (24)). The grain size shows no effect on the elastic limit, but significantly affects the flow stress at the plastic deformation stage. While all copper polycrystal show strain hardening, the strain hardening rate increases as the grain size decreases, which coincides with the experimental results and the simulation results obtained by Haouala et al. (Haouala et al., 2020b; Haouala et al., 2018). Since the simulation results with initial dislocation density of $1.2\times10^{12}/\text{m}^2$ fit well with the experimental results, the following analyses on the homogeneously-grained copper polycrystals are based on these results.

4.3. Grain size effect

Before studying the strain hardening of gradient grained materials, homogeneously-grained counterparts with grain sizes ranging from 5 μm to 80 μm are firstly investigated to figure out the dependencies of GND-related hardening on grain size. Fig. 8 shows the simulated true stress-strain curves of the copper polycrystals; the results without considering back stress are also shown for comparison. It is clear that for copper with grain size larger than 20 μm, the simulation results with and without back stress are almost identical. With the decrease of grain size, the discrepancy between the stress-strain curves with and without back stress becomes more and more obvious. Therefore, in copper with large grain sizes, the GND-induced kinematic hardening hardly contributes to their strain hardening, while the GND-induced kinematic hardening becomes more and more pronounced with decreasing grain size. This conclusion agrees with experimental results (Gao et al., 2022; Mahato et al., 2016; Vinogradov et al., 1997), where metals with smaller grain sizes showed a stronger Bauschinger effect.

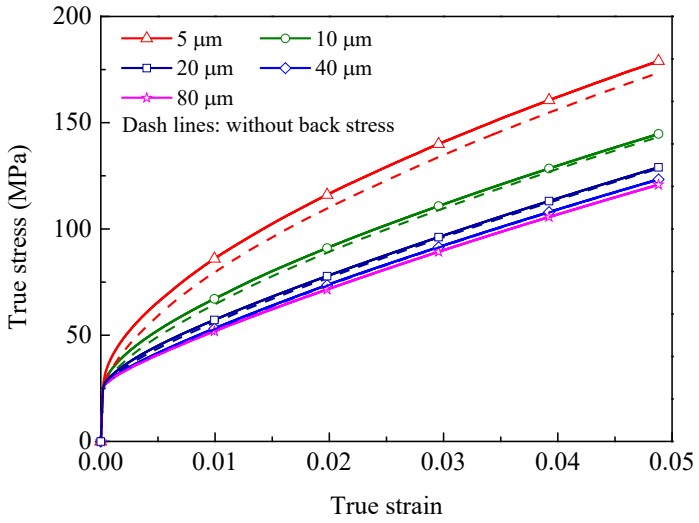

Fig. 8. Simulation results for copper with grain sizes changing from 5 μm to 80 μm, the results without considering back stress are also shown.

The above findings can be understood from two different points of view: (1) Physically, back stress comes from the spatially heterogeneous distribution of GNDs. In the initial deformation stage, back stress comes from the pileup of GNDs at GBs. In the subsequent deformation stage, dislocation structures such as cells and walls also lead to the heterogeneous distribution of dislocations, which further enhances back stress. In this work, the formation of dislocation structures during plastic deformation is not considered due to the limited strain range, so the heterogeneities come mainly from the slip discontinuities (pileups) at GBs. Therefore, back stress comes into effect at the initial deformation stage and does not increase during further deformation. (2) From the point of view of model prediction, Eq. (26) manifests that back stress is controlled by the gradient of GND density. Essentially, it is the effect of the second-order gradient of strain. In the conventional strain gradient theory, an internal length scale is introduced for dimension equilibrium. When the sample size is of the same order of magnitude as the internal length scale, the strain gradient comes into effect, and the strain gradient effect increases with the decrease of sample size, known as "smaller is stronger" (Fleck et al., 1994; Voyiadjis and Song, 2019). In Eq. (26), the dominant length scale is the mean dislocation spacing $1/\sqrt{\rho}$. Similar to the (first-order) strain gradient theory, when the spacing of the barriers constraining dislocation movement is also of the order of $1/\sqrt{\rho}$, the back stress effect becomes obvious. For the current simulations, GBs act as the primary constraints for dislocation motion, so GND-induced kinematic hardening is stronger for grains with smaller sizes.

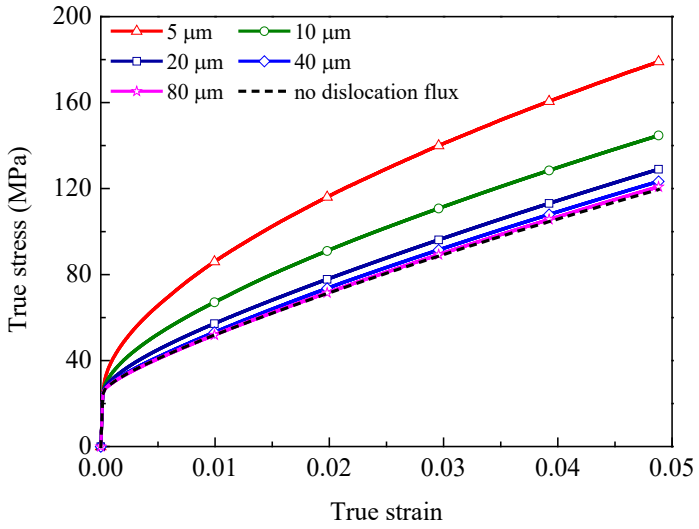

Fig. 9. Simulation results for copper with grain sizes changing from 5 μm to 80 μm, the results without dislocation flux are also shown.

Fig. 9 shows the comparison of the simulated true stress-strain curves with and without considering dislocation flux for copper with grain sizes ranging from 5 μm to 80 μm. It is evident that with decreasing grain size, the difference between the results with and without dislocation flux becomes larger and larger, which coincides well with that obtained in (Haouala et al., 2020b), where a lower-order strain gradient CP model was employed. Note that the back stress is calculated through the gradient of GND density, so the effects of the dislocation flux term simultaneously include the contributions of back stress and GNDs themselves. To study their individual influence on the strain hardening behavior, we use three steps to obtain the hardening from back stress and GNDs themselves. I. Fig. 8 gives the simulation results without including back stress. Therefore, by comparing the stress-strain curves with those considering back stress, kinematic hardening can be obtained. II. Fig. 9 plots the simulation results without including dislocation flux, and the constitutive model degenerates into a local model. Therefore, the nonlocal effects, including the GND-induced forest hardening (isotropic one) and GND-induced kinematic hardening, are absent. By comparing the stress-strain curves with those considering dislocation flux, the overall GND hardening and kinematic hardening can be obtained. III. By further calculating the difference between the results obtained from step I and step II, the kinematic hardening and GND hardening can be separated. The final results are shown in Fig. 10.

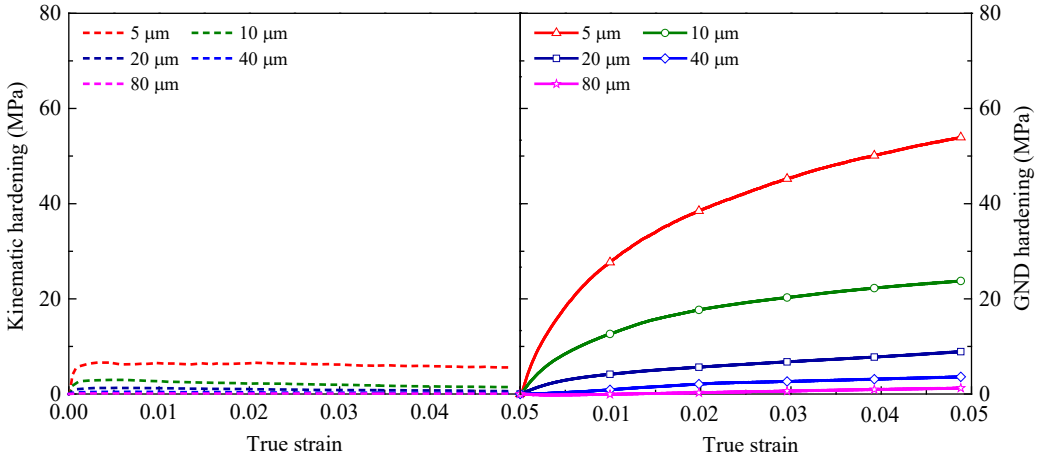

Fig. 10. GND-induced kinematic hardening and GND hardening in copper with grain sizes in the range of 5 μm to 80 μm.

Fig. 10 indicates that the GND-induced kinematic hardening emerges at the onset of plastic deformation and tends to saturate at an early deformation stage (less than 1%), which agrees with experimental findings (Cheng et al., 2018) on gradient nanotwinned copper. In comparison, the GND hardening increases gradually with the increase of strain. Moreover, GND hardening is stronger than GND-induced kinematic hardening. When the grain size is larger than 20 μm, the GND-related effects can be neglected. Therefore, conclusions can be drawn from the results in Figs. 8-10 that the smaller the grain size is, the stronger the GND hardening and GND-induced kinematic hardening are; GND-induced kinematic hardening emerges in the initial deformation stage and quickly reaches saturation, while GND hardening increases gradually in the deformation range of concern.

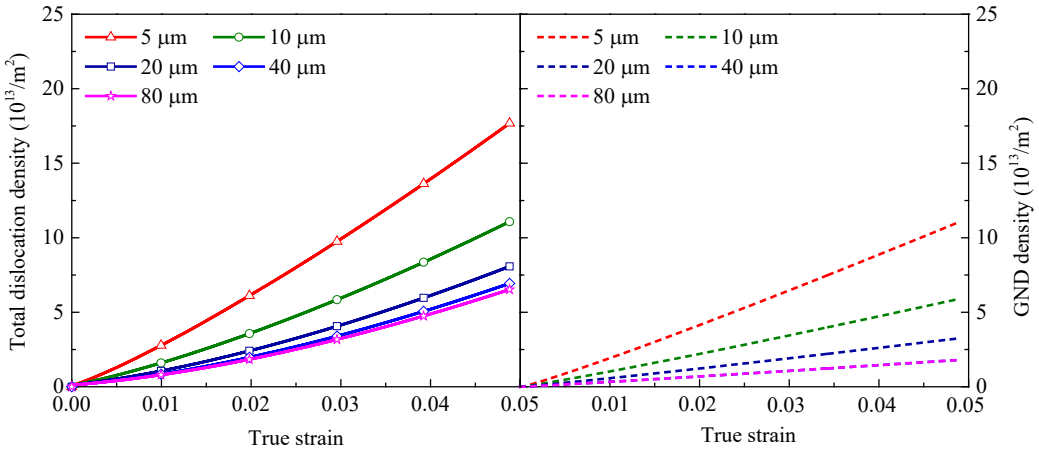

Fig. 11. Evolution of the total dislocation densities and GND densities for copper with different grain sizes.

To further understand the effect of GNDs on the deformation behavior of copper polycrystals,

Fig. 11 exhibits the evolution of total dislocation densities and GND densities for polycrystals with different grain sizes. The total dislocation density is calculated as $\rho_{\text{Total}}=\sum_{\alpha=1}^{12}\left(\rho_{\text{e}}^{\alpha}+\rho_{\text{s}}^{\alpha}\right)$. The GND densities are calculated as $\rho_{\Delta\text{e}}^{\alpha}=\rho_{\text{e+}}^{\alpha}-\rho_{\text{e–}}^{\alpha}$ and $\rho_{\Delta\text{s}}^{\alpha}=\rho_{\text{s+}}^{\alpha}-\rho_{\text{s–}}^{\alpha}$ for edge and screw type, respectively. So the GND density can be either positive or negative on a slip system. For comparison purposes, the GND density depicted here is calculated as $\rho_{\text{GND}}=\sum_{\alpha=1}^{12}\left(\left|\rho_{\Delta\text{e}}^{\alpha}\right|+\left|\rho_{\Delta\text{s}}^{\alpha}\right|\right)$. Fig. 11 demonstrates that in the investigated range of grain sizes (from 5 μm to 80 μm) and strain (0-5%), the smaller the grain size is, the higher the total dislocation density and GND density are. Moreover, both of them increase nearly linearly with strain due to rapid dislocation storage in the grain interior, which agrees with the experimental results (Zhang et al., 2020) and constitutive modeling results (Li and Soh, 2012).

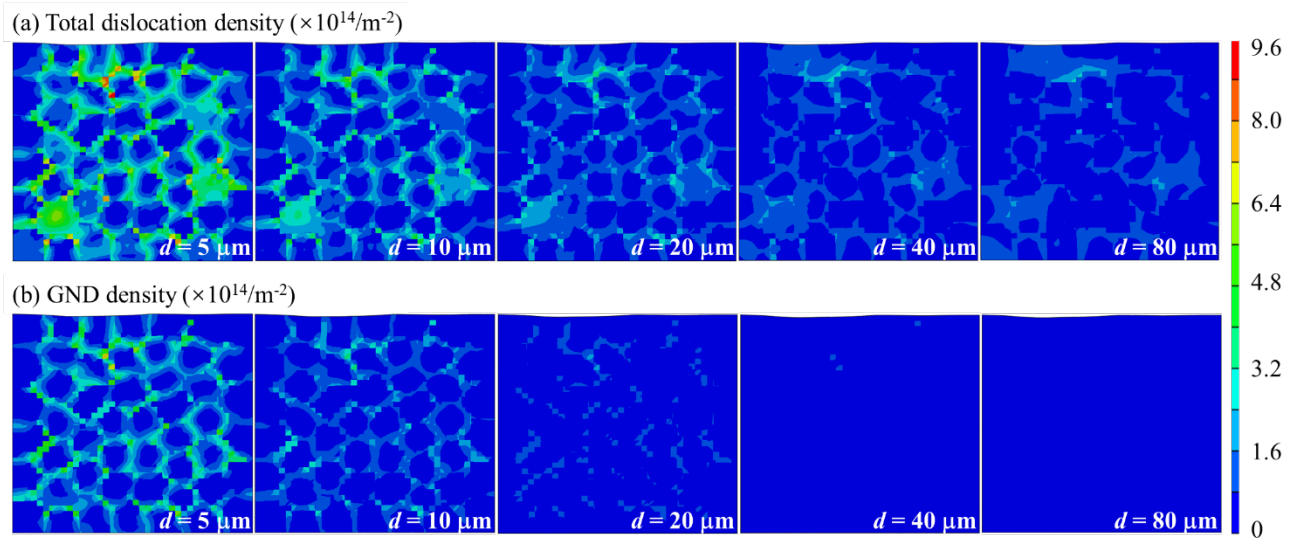

Fig. 12. The contours of (a) total dislocation density and (b) GND density for copper with different grain sizes at a true strain of ~5%.

Fig. 12 depicts the contours of total dislocation density and GND density for copper polycrystals with different grain sizes at a true strain of ~5%. Fig. 12(a) shows that the total dislocation densities near the GB are much higher than those in the grain interior. With the increase of grain size, the dislocation density decreases, and the density differences in the GB region and grain interior become smaller and smaller, indicating that the deformation in copper with larger grain size is more homogeneous. Fig. 12(b) shows that the GNDs accumulate close to the GBs, manifesting that the CPFEM framework, in combination with the GB model, can well describe the role of GBs as obstacles to dislocation motion. The GND densities in copper polycrystals with

smaller grains are higher than those with larger grains, and the GND densities in the GB region of smaller grains are also higher than those of larger grains.

5. Uniaxial tensile response of gradient grained copper

5.1. Finite element model

The effects of GNDs and back stress on the strain hardening of homogeneous copper polycrystals have been well understood based on the results shown in section 4. In this section, the tensile deformation of gradient grained copper is simulated to investigate the GND hardening and GND-induced kinematic hardening in gradient grained materials. In our previous work (Lu et al., 2019b), it is theoretically estimated that there are around 120000 grains even in the two-dimensional Voronoi tessellation construction for the gradient grained copper experimentally studied by Fang et al. (2011), which has been chosen as a benchmark work for simulation. This polycrystalline aggregate can not be handled computationally even using a phenomenologically-based model. Instead, homogenization schemes that endow each material point with several grains can be adopted to deal with the high computational demands (Lu et al., 2019b), and the macroscopic mechanical response of the gradient grained materials can be obtained. However, the motivation of this work is to study the underlying mechanisms behind the phenomenon. Therefore, a sandwich-structured gradient-grained copper is considered, whose grain number and grain size distribution are similar to those adopted by Zeng et al. (2015). Due to the symmetry, only 1/2 of the model is constructed for simulation, which comprises 84 grains, as shown in Fig. 13. The mesh convergence study shown in Appendix A demonstrates that a mesh resolution of $d/6$ (i.e., 36 meshes for each grain, which is larger than 32 meshes used in the homogeneous polycrystals) is sufficiently high for the homogeneous polycrystals studied. Therefore, the mesh in each layer of the gradient grained model is refined to be $d/6$ (which leads to a total mesh number of 2952) so that the calculation don't suffer from a mesh problem. Similar to the simulation of homogeneously-grained copper, a single layer geometric model was employed, assuming plane strain deformation.

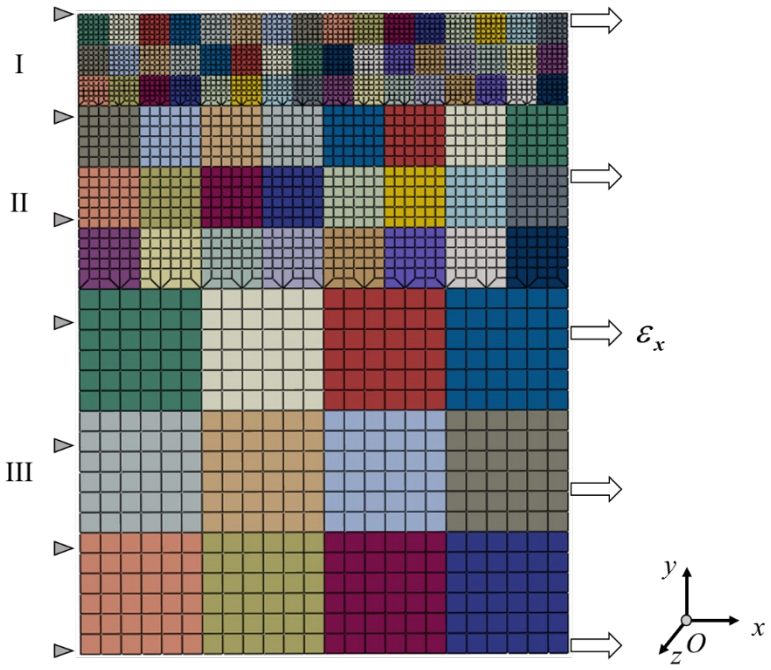

Fig. 13. Finite element model of the gradient grained polycrystal. Different colors represent grains with different orientations.

The geometric model was divided into three layers (I, II, III), with each layer being endowed with a specific grain size. If the smallest grain size is d, then the grain size distribution along y-direction is d, $2d$ and $4d$. In this investigation, d is taken to be 5 μm, so the overall geometrical size of the model is 80 μm×105 μm (x×y). Uniaxial tension was applied in the x-direction at a strain rate of $6\times10^{-4}/s$, all nodes' displacements along z-direction were constrained to be zero. In order to eliminate the randomness induced by the grain orientation effect, three sets of simulations with different grain orientations were performed; the distribution curves of internal state variables and stress-strain curves shown in the following sections were obtained by averaging these results.

5.2. Uniaxial tensile response of gradient grained copper

In this section, the distributions of several internal state variables, such as total dislocation density, GND density and back stress, are first analyzed to understand the deformation features of the gradient grained material. Then GND hardening and GND-induced kinematic hardening are studied to figure out their influences on the mechanical response of gradient grained copper.

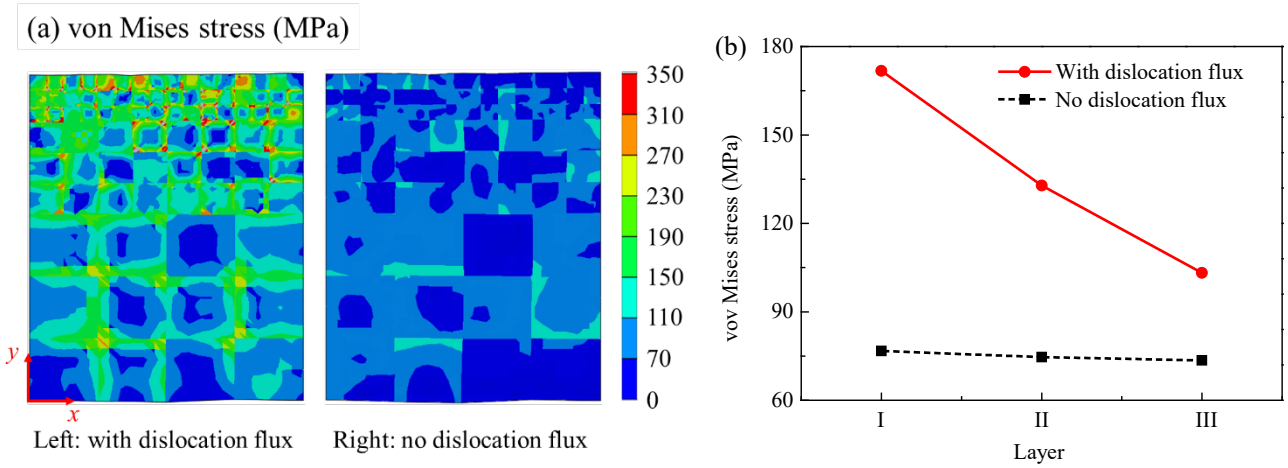

Fig. 14. (a) Contours of von Mises stress with and without considering dislocation flux at a true strain of ~5%, (b) average von Mises stress in each layer.

Figs. 14(a) and 14(b) show the contours of von Mises stress and the average stress distribution in each layer for gradient grained copper at a true strain of ~5%. The results without considering dislocation flux are also shown for comparison. For the latter case, the stress contours are more homogeneous than those considering flux/GND effects. They show no systematic differences between the grain interiors and the regions near the GBs. If dislocation flux is not considered, the average stress level in the different layers does not depend on the grain size and shows a flat distribution, as shown in Fig. 14(b). For the simulation results considering dislocation transport which leads to GND accumulation at GBs, the average von Mises stress decreases with increasing grain size. Furthermore, The stresses in all layers are higher than those without GND effects, and stress concentrations emerge at the GBs.

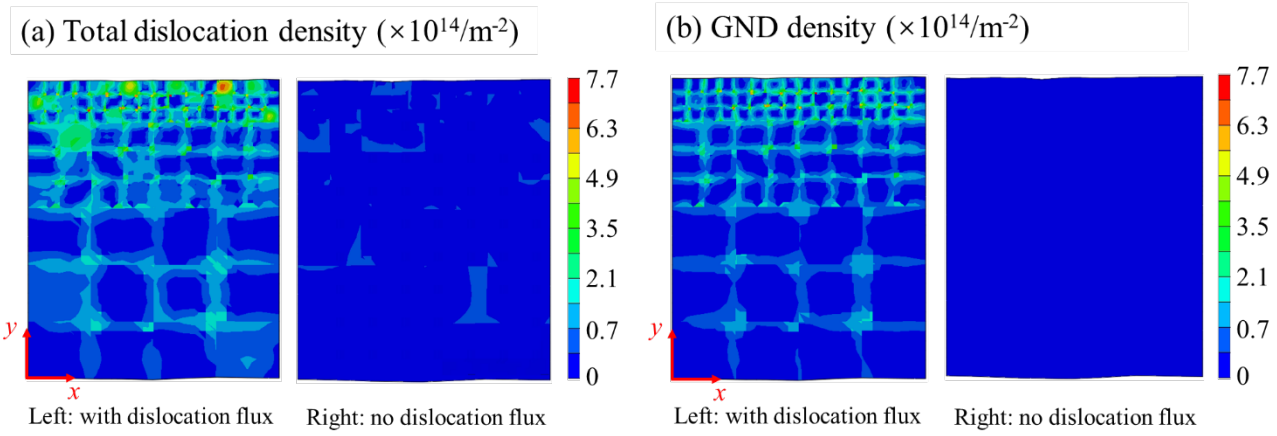

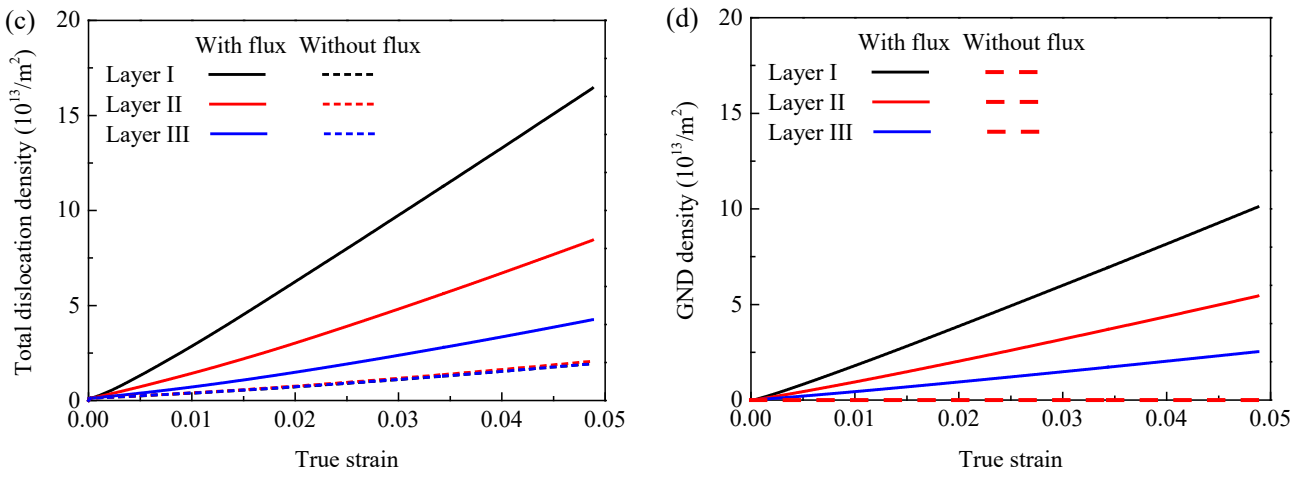

Fig. 15. Contours of (a) the total dislocation density and (b) GND density in the gradient grained copper at a true strain of ~5%; the results without considering dislocation flux are also shown. Evolution of (c) the total dislocation density and (d) GND density in each layer during deformation.

Figs. 15(a) and 15(b) give the contours of the total dislocation density and GND density at a true strain of ~5%, the simulation results without considering dislocation flux are also shown. Similar to the distribution of von Mises stress, both the total dislocation density and GND density show a gradient distribution when the flux term is involved, and dislocations accumulate preferentially at the grain boundaries. The distribution of GND density also coincides with the experimental observation (Hasan et al., 2019), i.e., GND density decreases from small grains to large grains in gradient grained materials. In contrast, the total dislocation density shows no gradient along the depth direction for the simulation results without dislocation flux, and dislocation accumulation has no systematic difference between the grain interiors and the near-GB regions. Moreover, since the non-locality of the CP model is realized through introducing a flux term, by which the dislocation information (dislocation density) exchange among material points can be obtained. If the dislocation flux term is not considered, then we only have the dislocation multiplication, annihilation and change of the dislocation state in one material point. The latter mechanisms only lead to the evolution of SSDs. Therefore, the GND density is zero when dislocation flux is absent, as shown in Fig. 15(b). Figs. 15(c) and 15(d) plot the total dislocation density and GND density evolution in each layer for the simulations with and without dislocation flux. When dislocation flux is included, the total dislocation density evolution shows an obvious difference in each layer, i.e., it increases more rapidly in the layer with smaller grain size. The same tendency is found for the evolution of GND density. In

contrast, for the results without dislocation flux, the dislocations only comprise the SSDs, and the dislocation density develops in almost the same way in each layer. As a result, the obtained total dislocation densities without dislocation flux are always lower than those considering dislocation flux.

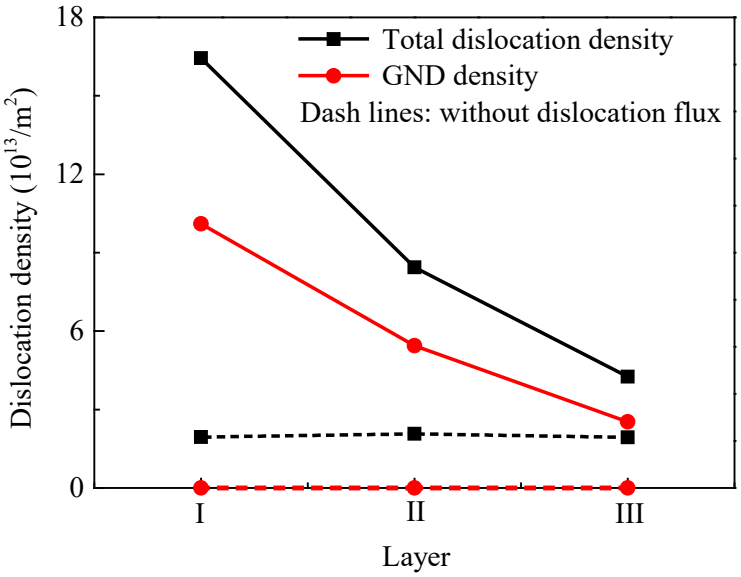

Fig. 16. Distributions of the total dislocation density and GND density in each layer of the gradient grained copper.

Fig. 16 further quantitatively depicts the average values of the two kinds of dislocation densities in each layer. The average dislocation densities decrease from the surface to the core region. The average total dislocation densities in each layer are 15.6×10^{13}/m^2, 8.6×10^{13}/m^2, 4.1×10^{13}/m^2; while those of GND densities are 10.0×10^{13}/m^2, 5.3×10^{13}/m^2 and 2.5×10^{13}/m^2. The GND densities account for 64.1%, 61.6% and 60.9% in each layer, demonstrating that with the decrease of grain size, the contribution of GND density to the total dislocation density increases. Thus the GND hardening is more significant in materials with smaller grains.

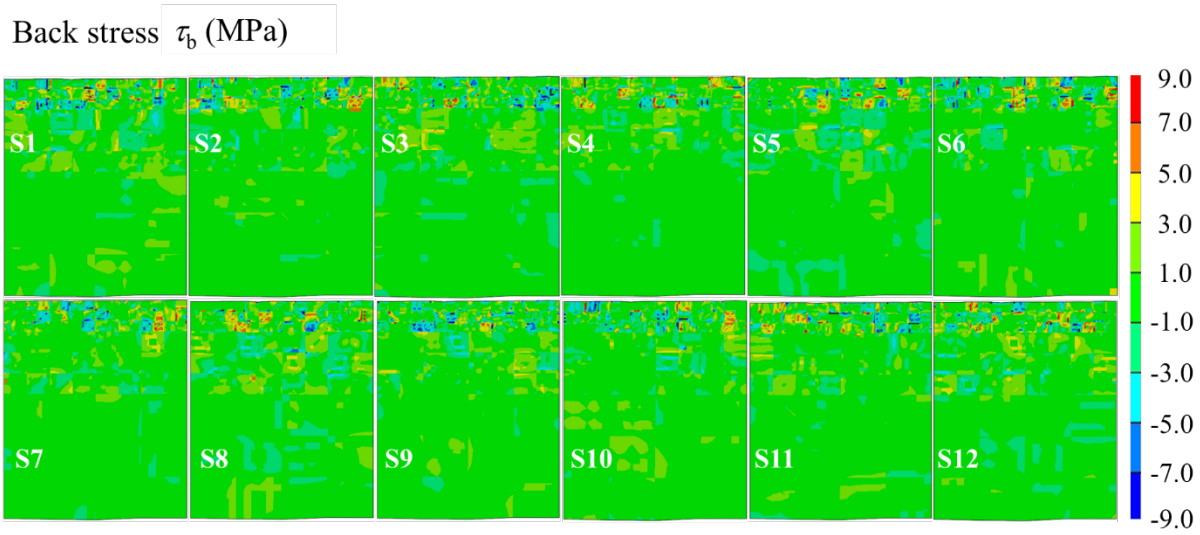

Fig. 17. Distributions of back stress on the 12 slip systems in the gradient grained copper at a true strain of ~5%.

Fig. 17 shows the distribution of back stress on the 12 slip systems at a true strain of ~5%. Similar to the distributions of von Mises stress, GND density and total dislocation density, the back stress increases with decreasing grain size, which is in accordance with the true stress-strain curves shown in Fig. 8 and experimental measurements (Gao et al., 2022; Mahato et al., 2016; Vinogradov et al., 1997). The results also indicate that back stress from the smaller grains is a non-negligible factor when discussing the GND-induced kinematic hardening in gradient grained material.

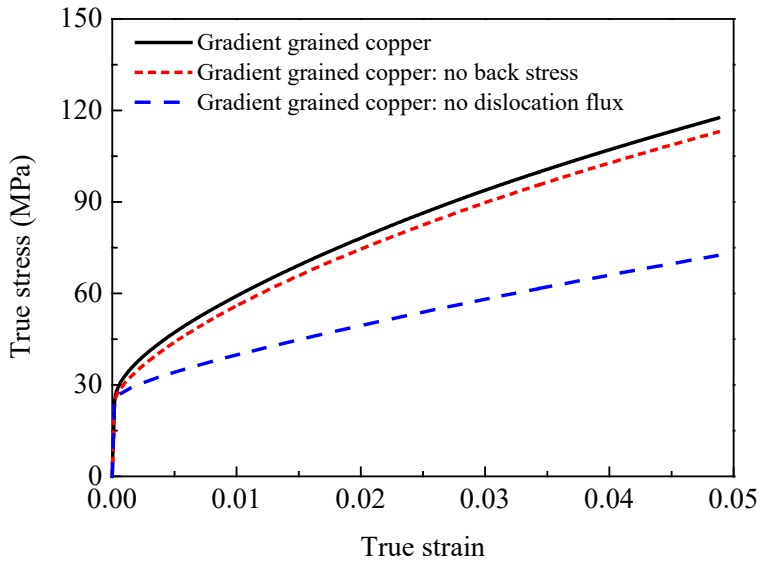

Fig. 18. Simulated uniaxial tensile response of the gradient grained copper, the results without considering back stress and dislocation flux are also shown for comparison.

Fig. 18 gives the simulated stress-strain curves for the gradient grained copper. Simulation results without considering back stress and dislocation flux are also shown for comparison. In the simulated gradient grained copper, the effect of back stress is weaker. The contribution of GND hardening increases gradually with increasing strain. The effect of GND density is stronger than that of the back stress in gradient grained copper, which corresponds to the conclusions drawn from the results for homogeneous copper. The discrepancy in the stress-strain curves with and without including dislocation flux is very similar to that obtained by Haouala et al. (Haouala et al., 2020b; Haouala et al., 2018). Note that the grain size in the simulated gradient grained copper is set to be fairly large due to restrictions of computation efficiency; it is expected that both the back stress and GND density will have significant effects on the strain hardening of gradient grained copper with nanograined surface layers, such as the gradient nano-grained metals reported in experiments (Cheng et al., 2018; Yang et al., 2016).

6. Conclusions

The GND-related hardening mechanisms in homogeneously-grained polycrystals and gradient grained FCC metals are studied using a dislocation density-based nonlocal CPFEM model. Introducing the flux term in the model enables the dislocation density exchange among material points, which renders the model nonlocal. A back stress model characterizing the effect of the heterogeneous distribution of GNDs is constructed for studying the kinematic hardening behavior. Specifically, the interaction between dislocations and GBs is explicitly considered in the current work by setting boundary conditions for the dislocation flux based on the geometrical and mechanical criteria. CPFEM simulations of homogeneously-grained copper quantitatively capture the Hall-Petch effect due to the accumulation of GNDs at grain boundaries. It is shown that smaller grain size leads to higher GND density and back stress. The back stress increases rapidly during the initial deformation stage and shows no obvious increase under further loading, while the GND hardening increases gradually with the increase of strain. CPFEM simulations of gradient grained copper reproduce its salient deformation features, such as the gradient distribution of stress, total dislocation density, GND density, and back stress. Furthermore, small grains in gradient grained materials contribute significantly to GND-related hardening. We emphasize that all these features are captured, in a formulation including dislocation flux, without the necessity for introducing any explicit grain size-dependent terms into the constitutive equations. This work is helpful for understanding the strengthening mechanisms of gradient grained materials as well as other kinds of heterogeneously-grained materials.

Acknowledgments

This work was funded by the National Natural Science Foundation of China (Grant No. 11872321, 11672251 and 12192214). M. Zaiser also acknowledges support by DFG under grant Za 171 13-1 and the Chinese State Administration of Foreign Experts Affairs under Grant no. G2021166001L.

Appendix. Mesh convergence study

To demonstrate that the mesh resolution is sufficiently high for all cases studied in this work, the 2D RVE for the homogeneously-grained copper polycrystals in Fig. 6 is generated with different mesh numbers: 400, 1024, 1600 and 2500, using Neper. The tensile stress-strain curves of the homogeneously-grained copper polycrystals with different grain sizes using these mesh resolutions are shown in Fig. A1 below.

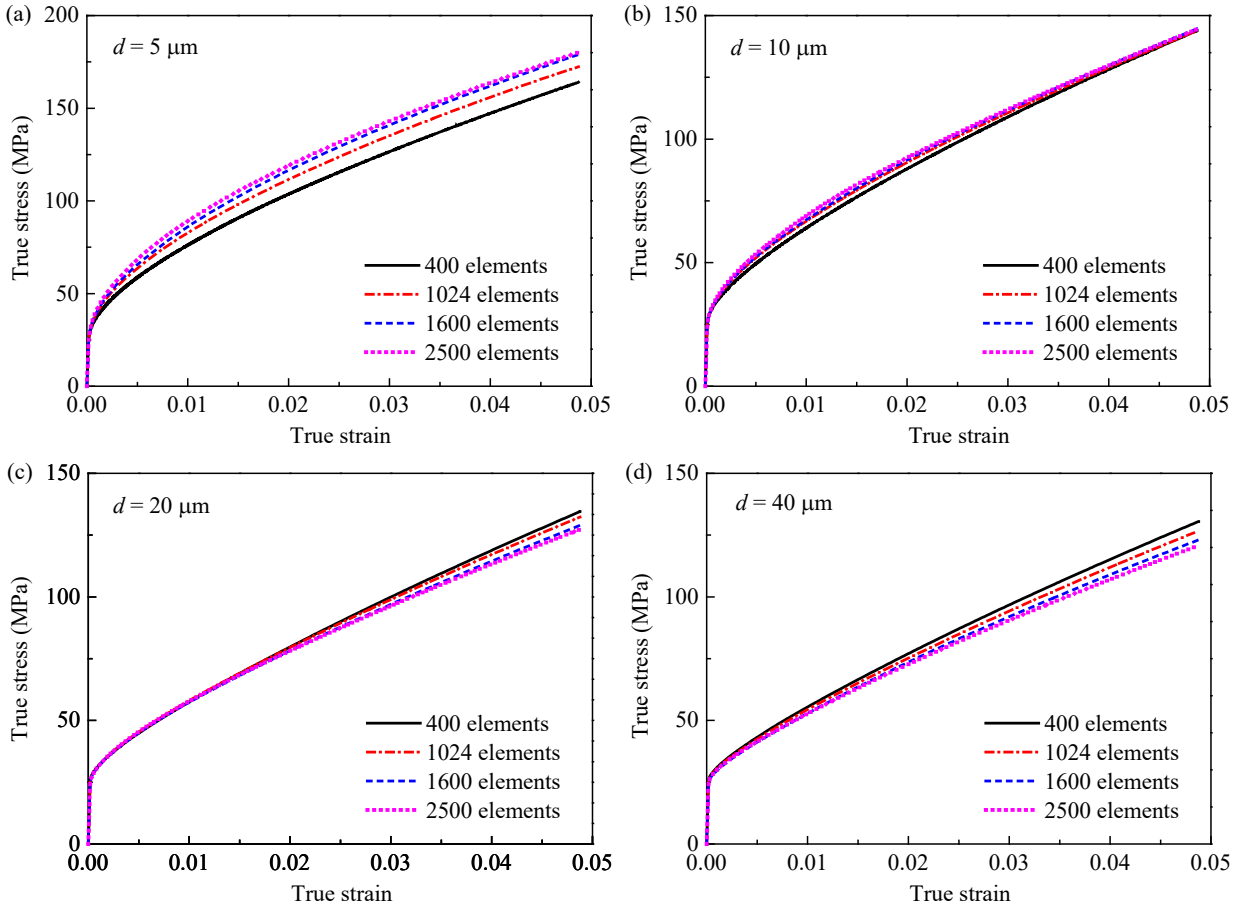

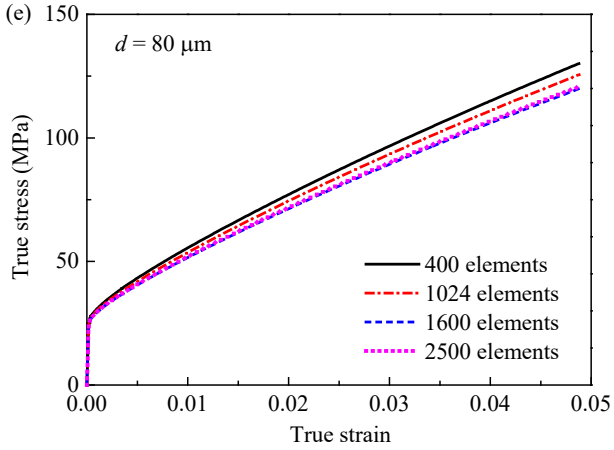

Fig. A1. Simulation results of the homogeneously-grained copper polycrystals with different grain sizes using the finite element models with different mesh resolutions.

The results indicate that the difference in the stress-strain curves becomes smaller and smaller with increasing the element number. As the element number increases from 1600 to 2500, the stress-strain curves nearly overlap for all cases studied. Therefore, to ensure the accuracy of the results and reduce the computation cost simultaneously, 1600 (40×40) elements are used to mesh the RVEs.

References

Acharya, A., Bassani, J.L., Beaudoin, A., 2003. Geometrically necessary dislocations, hardening, and a simple gradient theory of crystal plasticity. Scr. Mater. 48, 167-172.

Acharya, A., Beaudoin, A.J., 2000. Grain-size effect in viscoplastic polycrystals at moderate strains. Journal of the Mechanics and Physics of Solids 48, 2213-2230.

Agius, D., Kareer, A., Mamun, A.A., Truman, C., Collins, D.M., Mostafavi, M., Knowles, D., 2022. A crystal plasticity model that accounts for grain size effects and slip system interactions on the deformation of austenitic stainless steels. Int. J. Plast. 152, 103249.

Alizadeh, R., Peña-Ortega, M., Bieler, T.R., Llorca, J., 2020. A criterion for slip transfer at grain boundaries in Al. Scr. Mater. 178, 408-412.

Armstrong, R., Codd, I., Douthwaite, R.M., Petch, N.J., 1962. The plastic deformation of polycrystalline aggregates. Philosophical Magazine 7, 45-58.

Arsenlis, A., Parks, D.M., Becker, R., Bulatov, V.V., 2004. On the evolution of crystallographic dislocation density in non-homogeneously deforming crystals. Journal of the Mechanics and Physics of Solids 52, 1213-1246.

Ashby, M.F., 1970. The deformation of plastically non-homogeneous materials. Philosophical Magazine 21, 399-424.

Bargmann, S., Ekh, M., Runesson, K., Svendsen, B., 2010. Modeling of polycrystals with gradient crystal plasticity: A comparison of strategies. Philosophical Magazine 90, 1263-1288.

Bayerschen, E., McBride, A.T., Reddy, B.D., Böhlke, T., 2016. Review on slip transmission criteria in experiments and crystal plasticity models. Journal of Materials Science 51, 2243-2258.

Bieler, T.R., Alizadeh, R., Peña-Ortega, M., Llorca, J., 2019. An analysis of (the lack of) slip transfer between near-cube oriented grains in pure Al. Int. J. Plast. 118, 269-290.

Bulatov, V.V., Reed, B.W., Kumar, M., 2014. Grain boundary energy function for fcc metals. Acta Mater. 65, 161-175.

Chen, X., Han, Z., Li, X.Y., Lu, K., 2020. Friction of stable gradient nano-grained metals. Scr. Mater. 185, 82-87.

Cheng, Z., Bu, L., Zhang, Y., Wu, H., Zhu, T., Gao, H., Lu, L., 2022. Unraveling the origin of extra strengthening in gradient nanotwinned metals. Proceedings of the National Academy of Sciences 119, e2116808119.

Cheng, Z., Zhou, H., Lu, Q., Gao, H., Lu, L., 2018. Extra strengthening and work hardening in gradient nanotwinned metals. Science 362.

Cheong, K.S., Busso, E.P., Arsenlis, A., 2005. A study of microstructural length scale effects on the behaviour of FCC polycrystals using strain gradient concepts. Int. J. Plast. 21, 1797-1814.

Dai, H., 1997. Geometrically-necessary dislocation density in continuum plasticity theory, FEM implementation and applications, Dept. of Mechanical Engineering. Massachusetts Institute of Technology.

Ding, J., Li, Q., Li, J., Xue, S., Fan, Z., Wang, H., Zhang, X., 2018. Mechanical behavior of structurally gradient nickel alloy. Acta Mater. 149, 57-67.

Dunne, F.P.E., Rugg, D., Walker, A., 2007. Lengthscale-dependent, elastically anisotropic, physically-based hcp crystal plasticity: Application to cold-dwell fatigue in Ti alloys. Int. J. Plast. 23, 1061-1083.

Espinosa, H.D., Panico, M., Berbenni, S., Schwarz, K.W., 2006. Discrete dislocation dynamics simulations to interpret plasticity size and surface effects in freestanding FCC thin films. Int. J. Plast. 22, 2091-2117.

Essmann, U., Mughrabi, H., 1979. Annihilation of dislocations during tensile and cyclic deformation and limits of dislocation densities. Philos. Mag. A 40, 731-756.

Evers, L.P., Brekelmans, W.A.M., Geers, M.G.D., 2004a. Non-local crystal plasticity model with intrinsic SSD and GND effects. Journal of the Mechanics and Physics of Solids 52, 2379-2401.

Evers, L.P., Brekelmans, W.A.M., Geers, M.G.D., 2004b. Scale dependent crystal plasticity framework with dislocation density and grain boundary effects. International Journal of Solids and Structures 41, 5209-5230.

Evers, L.P., Parks, D.M., Brekelmans, W.A.M., Geers, M.G.D., 2002. Crystal plasticity model with enhanced hardening by geometrically necessary dislocation accumulation. Journal of the Mechanics and Physics of Solids 50, 2403-2424.

Fan, H., Li, Z., Huang, M., Zhang, X., 2011. Thickness effects in polycrystalline thin films: Surface constraint versus interior constraint. International Journal of Solids and Structures 48, 1754-1766.

Fang, Q., Li, L., Li, J., Wu, H., 2018. Strengthening mechanism of gradient nanostructured body-centred cubic iron film: From inverse Hall-Petch to classic Hall-Petch. Computational Materials Science 152, 236-242.

Fang, T.H., Li, W.L., Tao, N.R., Lu, K., 2011. Revealing extraordinary intrinsic tensile plasticity in gradient nano-grained copper. Science 331, 1587-1590.

Fleck, N.A., Muller, G.M., Ashby, M.F., Hutchinson, J.W., 1994. Strain gradient plasticity: Theory and experiment. Acta Metall. Mater. 42, 475-487.

Gao, S., Yoshino, K., Terada, D., Kaneko, Y., Tsuji, N., 2022. Significant Bauschinger effect and back stress strengthening in an ultrafine grained pure aluminum fabricated by severe plastic deformation process. Scr. Mater. 211, 114503.

Geers, M.G.D., Peerlings, R.H.J., Hoefnagels, J.P.M., Kasyanyuk, Y., 2009. On a proper account of first- and second-order size effects in crystal plasticity. Adv. Eng. Mater. 11, 143-147.

Ghorbani Moghaddam, M., Achuthan, A., Bednarcyk, B.A., Arnold, S.M., Pineda, E.J., 2017. Grain size-dependent crystal plasticity constitutive model for polycrystal materials. Mater. Sci. Eng. A. 703, 521-532.

Greer, J.R., Oliver, W.C., Nix, W.D., 2005. Size dependence of mechanical properties of gold at the micron scale in the absence of strain gradients. Acta Mater. 53, 1821-1830.

Grilli, N., 2016. Physics-based constitutive modelling for crystal plasticity finite element computation of cyclic

plasticity in fatigue. EPFL.
Grilli, N., Janssens, K.G., Nellessen, J., Sandlöbes, S., Raabe, D., 2018. Multiple slip dislocation patterning in a dislocation-based crystal plasticity finite element method. Int. J. Plast. 100, 104-121.
Groma, I., Bakó, B., 1998. Probability distribution of internal stresses in parallel straight dislocation systems. Physical Review B - Condensed Matter and Materials Physics 58, 2969-2974.
Groma, I., Csikor, F.F., Zaiser, M., 2003. Spatial correlations and higher-order gradient terms in a continuum description of dislocation dynamics. Acta Mater. 51, 1271-1281.
Gurtin, M.E., 2002. A gradient theory of single-crystal viscoplasticity that accounts for geometrically necessary dislocations. Journal of the Mechanics and Physics of Solids 50, 5-32.
Hansen, N., Ralph, B., 1982. The strain and grain size dependence of the flow stress of copper. Acta Metall. 30, 411-417.
Haouala, S., Alizadeh, R., Bieler, T., Segurado, J., LLorca, J., 2020a. Effect of slip transmission at grain boundaries in Al bicrystals. Int. J. Plast. 126, 102600.
Haouala, S., Lucarini, S., Llorca, J., Segurado, J., 2020b. Simulation of the Hall-Petch effect in FCC polycrystals by means of strain gradient crystal plasticity and FFT homogenization. Journal of the Mechanics and Physics of Solids 134, 103755.
Haouala, S., Segurado, J., Llorca, J., 2018. An analysis of the influence of grain size on the strength of FCC polycrystals by means of computational homogenization. Acta Mater. 148, 72-85.
Hasan, M., Liu, Y., An, X., Gu, J., Song, M., Cao, Y., Li, Y., Zhu, Y., Liao, X., 2019. Simultaneously enhancing strength and ductility of a high-entropy alloy via gradient hierarchical microstructures. Int. J. Plast. 123, 178-195.
Hochrainer, T., Sandfeld, S., Zaiser, M., Gumbsch, P., 2014. Continuum dislocation dynamics: Towards a physical theory of crystal plasticity. Journal of the Mechanics and Physics of Solids 63, 167-178.
Hua, F., Liu, D., Li, Y., He, Y., Dunstan, D.J., 2021. On energetic and dissipative gradient effects within higher-order strain gradient plasticity: Size effect, passivation effect, and Bauschinger effect. Int. J. Plast. 141, 102994.
Hull, D., Bacon, D.J., 2001. Introduction to dislocations. Butterworth-Heinemann.
Jamalian, M., Field, D.P., 2020. Effect of gradient microstructures on strengthening and toughening of AZ31. Mater. Sci. Eng. A. 771, 138615.
Jiang, J., Chen, Z., Ma, H., Xing, H., Li, X., 2022a. Strength-ductility synergy in heterogeneous-structured metals and alloys. Matter 5, 2430-2433.
Jiang, M., Devincre, B., Monnet, G., 2019. Effects of the grain size and shape on the flow stress: A dislocation dynamics study. Int. J. Plast. 113, 111-124.
Jiang, M., Fan, Z., Kruch, S., Devincre, B., 2022b. Grain size effect of FCC polycrystal: A new CPFEM approach based on surface geometrically necessary dislocations. Int. J. Plast. 150, 103181.
Kang, G., Kan, Q., 2017. Cyclic plasticity of engineering materials: experiments and models. John Wiley & Sons.
Kords, C., 2013. On the role of dislocation transport in the constitutive description of crystal plasticity. epubli GmbH Berlin.
Kubin, L., Devincre, B., Hoc, T., 2008. Modeling dislocation storage rates and mean free paths in face-centered cubic crystals. Acta Mater. 56, 6040-6049.
Lebensohn, R.A., Needleman, A., 2016. Numerical implementation of non-local polycrystal plasticity using fast Fourier transforms. Journal of the Mechanics and Physics of Solids 97, 333-351.
Lee, H.H., Park, H.K., Jung, J., Hwang, K.J., Kim, H.S., 2019a. Microstructural tailoring in reverse gradient-structured copper sheet using single-roll angular-rolling and subsequent annealing. Mater. Sci. Eng. A. 764, 138258.
Lee, H.H., Yoon, J.I., Park, H.K., Kim, H.S., 2019b. Unique microstructure and simultaneous enhancements of strength and ductility in gradient-microstructured Cu sheet produced by single-roll angular-rolling. Acta Mater. 166,

638-649.
Lee, T.C., Robertson, I.M., Birnbaum, H.K., 1989. Prediction of slip transfer mechanisms across grain boundaries. Scripta Metallurgica et Materialia 23, 799-803.
Leung, H.S., Leung, P.S.S., Cheng, B., Ngan, A.H.W., 2015. A new dislocation-density-function dynamics scheme for computational crystal plasticity by explicit consideration of dislocation elastic interactions. Int. J. Plast. 67, 1-25.
Li, J., Soh, A.K., 2012. Modeling of the plastic deformation of nanostructured materials with grain size gradient. Int. J. Plast. 39, 88-102.
Li, J., Weng, G., Chen, S., Wu, X., 2017. On strain hardening mechanism in gradient nanostructures. Int. J. Plast. 88, 89-107.
Li, J., Zhang, Q., Huang, R., Li, X., Gao, H., 2020a. Towards understanding the structure–property relationships of heterogeneous-structured materials. Scr. Mater. 186, 304-311.
Li, W., Yuan, F., Wu, X., 2015. Atomistic tensile deformation mechanisms of Fe with gradient nano-grained structure. AIP Advances 5, 087120.
Li, X., Lu, L., Li, J., Zhang, X., Gao, H., 2020b. Mechanical properties and deformation mechanisms of gradient nanostructured metals and alloys. Nature Reviews Materials, 1-18.
Li, Z., Hou, C., Huang, M., Ouyang, C., 2009. Strengthening mechanism in micro-polycrystals with penetrable grain boundaries by discrete dislocation dynamics simulation and Hall-Petch effect. Computational Materials Science 46, 1124-1134.
Lim, H., Lee, M.G., Kim, J.H., Adams, B.L., Wagoner, R.H., 2011. Simulation of polycrystal deformation with grain and grain boundary effects. Int. J. Plast. 27, 1328-1354.
Lin, Y., Pan, J., Zhou, H.F., Gao, H.J., Li, Y., 2018. Mechanical properties and optimal grain size distribution profile of gradient grained nickel. Acta Mater. 153, 279-289.
Liu, D., Dunstan, D.J., 2017. Material length scale of strain gradient plasticity: A physical interpretation. Int. J. Plast. 98, 156-174.
Liu, W., Liu, Y., Sui, H., Chen, L., Yu, L., Yi, X., Duan, H., 2020. Dislocation-grain boundary interaction in metallic materials: Competition between dislocation transmission and dislocation source activation. Journal of the Mechanics and Physics of Solids 145, 104158.
Liu, X., Yuan, F., Zhu, Y., Wu, X., 2018. Extraordinary Bauschinger effect in gradient structured copper. Scr. Mater. 150, 57-60.
Lu, K., 2014. Making strong nanomaterials ductile with gradients. Science 345, 1455-1456.
Lu, S., Zhang, B., Li, X., Zhao, J., Zaiser, M., Fan, H., Zhang, X., 2019a. Grain boundary effect on nanoindentation: A multiscale discrete dislocation dynamics model. Journal of the Mechanics and Physics of Solids 126, 117-135.
Lu, S., Zhao, J., Huang, M., Li, Z., Kang, G., Zhang, X., 2022. Multiscale discrete dislocation dynamics study of gradient nano-grained materials. Int. J. Plast. 156, 103356.
Lu, X., Zhang, X., Shi, M., Roters, F., Kang, G., Raabe, D., 2019b. Dislocation mechanism based size-dependent crystal plasticity modeling and simulation of gradient nano-grained copper. Int. J. Plast. 113, 52-73.
Lu, X., Zhao, J., Wang, Z., Gan, B., Zhao, J., Kang, G., Zhang, X., 2020. Crystal plasticity finite element analysis of gradient nanostructured TWIP steel. Int. J. Plast. 130, 102703.
Luscher, D.J., Bronkhorst, C.A., Alleman, C.N., Addessio, F.L., 2013. A model for finite-deformation nonlinear thermomechanical response of single crystal copper under shock conditions. Journal of the Mechanics and Physics of Solids 61, 1877-1894.
Luscher, D.J., Mayeur, J.R., Mourad, H.M., Hunter, A., Kenamond, M.A., 2016. Coupling continuum dislocation transport with crystal plasticity for application to shock loading conditions. Int. J. Plast. 76, 111-129.
Lyu, H., Hamid, M., Ruimi, A., Zbib, H.M., 2017. Stress/strain gradient plasticity model for size effects in

heterogeneous nano-microstructures. Int. J. Plast. 97, 46-63.

Lyu, H., Ruimi, A., Zbib, H.M., 2015. A dislocation-based model for deformation and size effect in multi-phase steels. Int. J. Plast. 72, 44-59.

Ma, A., Roters, F., Raabe, D., 2006. A dislocation density based constitutive model for crystal plasticity FEM including geometrically necessary dislocations. Acta Mater. 54, 2169-2179.

Ma, E., Zhu, T., 2017. Towards strength–ductility synergy through the design of heterogeneous nanostructures in metals. Mater. Today 20, 323-331.

Mahato, J.K., De, P.S., Sarkar, A., Kundu, A., Chakraborti, P.C., 2016. Effect of deformation mode and grain size on Bauschinger behavior of annealed copper. Int. J. Fatigue 83, 42-52.

Mayeur, J., Beyerlein, I., Bronkhorst, C., Mourad, H., 2015. Incorporating interface affected zones into crystal plasticity. Int. J. Plast. 65, 206-225.

Mayeur, J.R., Mourad, H.M., Luscher, D.J., Hunter, A., Kenamond, M.A., 2016. Numerical implementation of a crystal plasticity model with dislocation transport for high strain rate applications. Modell. Simul. Mater. Sci. Eng. 24, 045013.

Moering, J., Ma, X., Malkin, J., Yang, M., Zhu, Y., Mathaudhu, S., 2016. Synergetic strengthening far beyond rule of mixtures in gradient structured aluminum rod. Scr. Mater. 122, 106-109.

Orowan, E., 1934. Zur Kristallplastizität. I - Tieftemperaturplastizität und Beckersche Formel. Zeitschrift für Physik 89, 605-613.

Qin, S., Yang, M., Jiang, P., Wang, J., Wu, X., Zhou, H., Yuan, F., 2022. Designing structures with combined gradients of grain size and precipitation in high entropy alloys for simultaneous improvement of strength and ductility. Acta Mater. 230, 117847.

Quey, R., Dawson, P.R., Barbe, F., 2011. Large-scale 3D random polycrystals for the finite element method: Generation, meshing and remeshing. Computer Methods in Applied Mechanics and Engineering 200, 1729-1745.

Reuber, C., Eisenlohr, P., Roters, F., Raabe, D., 2014. Dislocation density distribution around an indent in single-crystalline nickel: Comparing nonlocal crystal plasticity finite-element predictions with experiments. Acta Mater. 71, 333-348.

Roters, F., 2011. Advanced material models for the crystal plasticity finite element method: development of a general CPFEM framework. Fachgruppe für Materialwissenschaft und Werkstofftechnik.

Roters, F., Diehl, M., Shanthraj, P., Eisenlohr, P., Reuber, C., Wong, S.L., Maiti, T., Ebrahimi, A., Hochrainer, T., Fabritius, H.O., Nikolov, S., Friák, M., Fujita, N., Grilli, N., Janssens, K.G.F., Jia, N., Kok, P.J.J., Ma, D., Meier, F., Werner, E., Stricker, M., Weygand, D., Raabe, D., 2019. DAMASK – The Düsseldorf Advanced Material Simulation Kit for modeling multi-physics crystal plasticity, thermal, and damage phenomena from the single crystal up to the component scale. Computational Materials Science 158, 420-478.

Rubio, R.A., Haouala, S., Llorca, J., 2019. Grain boundary strengthening of FCC polycrystals. J. Mater. Res. 34, 2263-2274.

Shao, C.W., Zhang, P., Wang, X.G., Wang, Q., Zhang, Z.F., 2019. High-cycle fatigue behavior of TWIP steel with graded grains: breaking the rule of mixture. Mater. Res. Lett.. 7, 26-32.

Shao, C.W., Zhang, P., Zhu, Y.K., Zhang, Z.J., Pang, J.C., Zhang, Z.F., 2017. Improvement of low-cycle fatigue resistance in TWIP steel by regulating the grain size and distribution. Acta Mater. 134, 128-142.

Vinogradov, A., Kaneko, Y., Kitagawa, K., Hashimoto, S., Stolyarov, V., Valiev, R., 1997. Cyclic response of ultrafine-grained copper at constant plastic strain amplitude. Scr. Mater. 36, 1345-1351.

Voyiadjis, G.Z., Song, Y., 2019. Strain gradient continuum plasticity theories: Theoretical, numerical and experimental investigations. Int. J. Plast. 121, 21-75.

Wang, Y., Yang, G., Wang, W., Wang, X., Li, Q., Wei, Y., 2017. Optimal stress and deformation partition in gradient

materials for better strength and tensile ductility: A numerical investigation. Sci. Rep. 7, 10954.
Wang, Y., Yang, M., Ma, X., Wang, M., Yin, K., Huang, A., Huang, C., 2018. Improved back stress and synergetic strain hardening in coarse-grain/nanostructure laminates. Mater. Sci. Eng. A. 727, 113-118.
Weng, G., 1983. A micromechanical theory of grain-size dependence in metal plasticity. Journal Of The Mechanics And Physics Of Solids 31, 193-203.
Wilkinson, A.J., Tarleton, E., Vilalta-Clemente, A., Jiang, J., Britton, T.B., Collins, D.M., 2014. Measurement of probability distributions for internal stresses in dislocated crystals. Appl. Phys. Lett. 105, 181907.
Wu, X., Jiang, P., Chen, L., Yuan, F., Zhu, Y.T., 2014a. Extraordinary strain hardening by gradient structure. Proc. Natl. Acad. Sci. U. S. A. 111, 7197.
Wu, X., Zhu, Y., 2017. Heterogeneous materials: a new class of materials with unprecedented mechanical properties. Mater. Res. Lett.. 5, 527-532.
Wu, X., Zhu, Y., 2021. Gradient and lamellar heterostructures for superior mechanical properties. MRS Bull. 46, 244-249.
Wu, X., Zhu, Y., Lu, K., 2020. Ductility and strain hardening in gradient and lamellar structured materials. Scr. Mater. 186, 321-325.
Wu, X.L., Jiang, P., Chen, L., Zhang, J.F., Yuan, F.P., Zhu, Y.T., 2014b. Synergetic Strengthening by Gradient Structure. Mater. Res. Lett.. 2, 185-191.
Wulfinghoff, S., Böhlke, T., 2015. Gradient crystal plasticity including dislocation-based work-hardening and dislocation transport. Int. J. Plast. 69, 152-169.
Xu, Y., 2021. A non-local methodology for geometrically necessary dislocations and application to crack tips. Int. J. Plast. 140, 102970.
Xu, Y., Ruebeling, F., Balint, D., Greiner, C., Dini, D., 2021. On the origin of microstructural discontinuities in sliding contacts: A discrete dislocation plasticity analysis. Int. J. Plast. 138, 102942.
Yang, M., Pan, Y., Yuan, F., Zhu, Y., Wu, X., 2016. Back stress strengthening and strain hardening in gradient structure. Mater. Res. Lett.. 4, 145-151.
Yang, X., Ma, X., Moering, J., Zhou, H., Wang, W., Gong, Y., Tao, J., Zhu, Y., Zhu, X., 2015. Influence of gradient structure volume fraction on the mechanical properties of pure copper. Mater. Sci. Eng. A. 645, 280-285.
Zaiser, M., Hochrainer, T., 2006. Some steps towards a continuum representation of 3D dislocation systems. Scr. Mater. 54, 717-721.
Zaiser, M., Moretti, P., 2005. Fluctuation phenomena in crystal plasticity - A continuum model. Journal of Statistical Mechanics: Theory and Experiment, 79-97.
Zaiser, M., Nikitas, N., Hochrainer, T., Aifantis, E.C., 2007. Modelling size effects using 3D density-based dislocation dynamics. Philosophical Magazine 87, 1283-1306.
Zaiser, M., Seeger, A., 2002. Chapter 56 Long-range internal stresses, dislocation patterning and work-hardening in crystal plasticity, in: Nabarro, F.R.N., Duesbery, M.S. (Eds.), Dislocations in Solids. Elsevier, pp. 1-100.
Zeng, Z., Li, X., Xu, D., Lu, L., Gao, H., Zhu, T., 2015. Gradient plasticity in gradient nano-grained metals. Extreme Mechanics Letters, 213-219.
Zhang, S., Liu, W., Wan, J., Misra, R.D.K., Wang, Q., Wang, C., 2020. The grain size and orientation dependence of geometrically necessary dislocations in polycrystalline aluminum during monotonic deformation: Relationship to mechanical behavior. Mater. Sci. Eng. A. 775, 138939.
Zhao, J., Kan, Q., Zhou, L., Kang, G., Fan, H., Zhang, X., 2019. Deformation mechanisms based constitutive modelling and strength-ductility mapping of gradient nano-grained materials. Mater. Sci. Eng. A. 742, 400-408.
Zhao, J., Lu, X., Liu, J., Bao, C., Kang, G., Zaiser, M., Zhang, X., 2021. The tension-compression behavior of gradient structured materials: A deformation-mechanism-based strain gradient plasticity model. Mech. Mater. 159,

103912.
Zhao, J., Lu, X., Yuan, F., Kan, Q., Qu, S., Kang, G., Zhang, X., 2020. Multiple mechanism based constitutive modeling of gradient nanograined material. Int. J. Plast. 125, 314-330.
Zhao, J., Zhang, B., Liu, D., Konstantinidis, A.A., Kang, G., Zhang, X., 2022. Generalized Aifantis strain gradient plasticity model with internal length scale dependence on grain size, sample size and strain. Acta Mechanica Sinica 38, 421188.
Zhou, K., Zhang, T., Liu, B., Yao, Y., 2018. Molecular dynamics simulations of tensile deformation of gradient nano-grained copper film. Computational Materials Science 142, 389-394.
Zhu, Y., Ameyama, K., Anderson, P.M., Beyerlein, I.J., Gao, H., Kim, H.S., Lavernia, E., Mathaudhu, S., Mughrabi, H., Ritchie, R.O., Tsuji, N., Zhang, X., Wu, X., 2021. Heterostructured materials: superior properties from hetero-zone interaction. Mater. Res. Lett.. 9, 1-31.
Zhu, Y., Wu, X., 2019. Perspective on hetero-deformation induced (HDI) hardening and back stress. Mater. Res. Lett.. 7, 393-398.
Zhu, Y., Wu, X., 2023. Heterostructured materials. Prog. Mater Sci. 131, 101019.